1. Introduction

1.1 Background

In the mining industry there are ever-present problems in maintaining structural stability of access roadways, belt roads, and numerous other underground headings and openings. Unstable roof conditions are common in underground coal mining environments. They are mainly the result of the layered structure of the sedimentary rocks encountered. Numerous methods are employed to stabilize these structures, particularly timbering and strapping via rock bolts. Structural problems around underground openings in the case of mines in hard rock are often associated with the blocky nature of the rock mass surrounding the opening. Thus, there is a need to quantify and monitor the stability of suspect zones of rock surrounding underground openings, particularly areas which are subject to damage from nearby blasting.

Conventional techniques for monitoring these areas include :

1) The traditional impact sounding method whereby a skilled miner strikes the suspect rock with a sounding bar and, based on his accumulated experience, can determine whether or not a suspect zone of rock is stable This technique is usually employed to detect (and subsequently remove) small scale areas of loosened rock. It can be considered as a subjective geophysical testing method.

2) Convergence tests for roof or wall structural behaviour based on the output from electrical displacement measuring devices such as LVDTs (linear voltage differential transformers) or, more commonly used, dial gauge readings of displacements between points on the walls, roof or floor

3) Observation of the effects of changing stresses in supporting timbers, i.e., cracking and splitting, and observation of changes in rock joint openings etc.

4) Microseismic monitoring of "active " regions of mines whereby correlations between changes in stress conditions and frequency of microseismic events are attempted.

Most of the monitoring practices are therefore relatively subjective with the exception of the convergence measurements (which give only point measurements) and the microseismic work. The microseismic techniques, particularly when employed at coal mines, are based largely on empirical results, i.e., the correlation of increasing event count with impending roof falls. Such correlations, when established (often tenuously) at a particular mine, are often unreliable when extrapolated to other locations. Accurate microseismic source location is a requisite of this technique although this is beset with difficulties. The major problems appear to be that of accounting for the highly anisotropic nature of the rock (particularly in the coal mine case), and the refraction and diffraction effects associated with the often complex mine layouts and geology. However, recent work in Canada in this area is showing great promise (Dr. Paul Young, Queen's University, Kingston, Canada, private communication).

The author therefore decided to investigate other methods, with a more rigorous geophysical base, of assessing structural integrity in underground rock masses. The first approach was to investigate the vibrational response of the walls of underground openings when defects, such as delaminations of sedimentary layers, were present. This work lead to a promising technique - that of vibrational signature analysis (Siggins and Enever, 1979). However, with it came the realisation that little was known of the vibrational modal behaviour of openings in intact rock. It was intuitively felt that modal behaviour of underground openings would be intimately associated with the presence of circulating surface (Rayleigh) waves which would be largely confined to the inner surface of the openings or tunnels.

A literature search on the interaction of elastic waves with cavities in elastic media revealed that a substantial amount of work had been done by authors such as Pao and Mow (1973) and Miklowitz (1980) which was applicable to the seismic response of underground tunnels. The emphasis had been placed on the interaction of incoming plane

compressional and shear waves with cylindrical and spherical openings in elastic materials. Little work had been done on the cavity wall response due to internal sources although the generation of transient Rayleigh waves circulating around the cavity circumference had been postulated.

The project thus proceeded along three major lines:

1) The development of an analytical description of the idealised problem of a localised source acting on the wall of a cavity in an elastic medium in order to clarify the physics involved in such an interaction.

2) Numerical simulation of the above problem based on dynamic Finite Element methods. This technique allows the analysis to be readily extended to cavities of arbitrary shape.

3) A program of experimental work, both in the field at mine sites and laboratory based.

The analytical work was commenced by the author with an attempt to solve the frequency equation (eigenvalues) for a cylindrical cavity in an infinite elastic medium. This work entailed a re-examination of the work of Viktorov (1958) where a "frequency equation " is described. It was recognised by the author that the roots of this equation are central to all elastic wave/cavity interactions.

Solutions up to the fifth eigenvalue (n=5) had appeared in the literature in various contexts, e.g., as poles of integral equations arising from the interaction of a compressional wavefront with a cavity. Viktorov's frequency equation was rarely mentioned in these works.

An attempt was made to solve the frequency equation using graphical methods as had other authors. However, it was realised that a more elegant solution should be

possible. Dr. A.N. Stokes of the CSIRO Division of Mathematics and Statistics was then approached for assistance in developing a solution method. Dr. Stokes provided a continued fractions expansion for the Hankel function ratios involved in the Viktorov equation A joint effort then resulted in a solution method based on a Newton-Raphson root finding approach. Eigenvalues up to n=10 and beyond were readily obtained to a high degree of accuracy. The results were then submitted for publication (Stokes and Siggins, 1987). In that publication the similarity of other author's expressions (with identical eigenvalues) to the Viktorov equation were pointed out. A knowledge of the eigenvalues for the cavity then readily leads to an analytical solution, based on a Fourier-Bessel series, for a localised source on a cavity wall. This solution was developed with the aid of Dr. Stokes and published in Geophysics (Siggins and Stokes, 1987).

Concurrent with the analytical development a time-domain numerical solution for a cylindrical cavity in an infinite elastic medium excited by a line source acting on the cavity wall was carried out by the author. The solution procedure consisted of a Dynamic Finite Element analysis, using step by step integration, followed by spectral analysis on the resulting waveforms. Spectral ratio techniques were then used to arrive at the cavity wall transfer functions.

At this stage the analytical solution had not been developed far enough to function as a check on the numerical solution. However, a computer program had been recently developed by the author's co-supervisor, Dr. Dane Blair, which evaluated, via a Fourier-Bessel series, the solution for cavity wall displacements arising from an incoming plane compressional wave. This program was made available to the author and with a small modification and by invoking seismic reciprocity principles it was possible to calculate the far-field waveform resulting from a pulse applied to the cavity wall. Thus, a check on the numerical solution was obtained.

The experimental work evolved from earlier work concerned with assessing coal mine roof stability via dynamic methods (Siggins, 1983). The dynamic response of the roof was found to be dominated by modal behaviour associated with the strong acoustic impedance contrasts in the sedimentary layering in the roof structure. Any resonances associated with standing Rayleigh waves were thought to be masked by these effects. Thus, an experimental program was commenced with the aim of investigating Rayleigh wave resonances in hard rock, i.e., in metalliferous mining environments where the geology is generally less complicated.

The majority of the experimental work in the field was performed in an access heading on the 17th level at the New Broken Hill Corporation Mine, Broken Hill, N.S.W. Additional measurements were made in the Hillgrove tunnel, Hillgrove Geophysical Observatory, Armidale, N.S.W.

These experiments were carried out with varying degrees of thoroughness due to the difficult environments and the poor condition of the rock at these sites. More closely controlled experimental work was carried out by the author in the laboratory on 0.15m diameter boreholes in a large granite block.

1.2 Objectives and description of the study

The long term aim of this project was to develop a geophysically based non-destructive test for underground openings in rock. The test was to be based on the generation of Rayleigh type elastic waves on the opening walls. Analytical extensions of Lamb's (1904) solution to that of Rayleigh waves on curved surfaces were initiated by Japanese workers such as Sezawa (1927) at the Earthquake Research Institute, University of Tokyo, in the late 1920's, but it was not until 1958 that Viktorov published his definitive paper on surface waves on convex and concave surfaces that the physics was clarified. Viktorov (1958) examined the existence of Rayleigh modes on convex surfaces in some detail and established the frequency equation for both convex and concave surfaces. However, he did not examine the convex case in the same detail, other than by showing that in both cases propagation is dispersive.

In the 1960's and 70's a great deal of interest was shown in the response of underground openings to seismic loading, no doubt prompted by the perceived need for structurally stable underground installations. Many papers were published during that period on the analysis of plane waves (both shear and compressional) impinging on cavities in elastic media. The most significant contributions were from Miklowitz (1967), Baron and Matthews (1961), Baron and Parnes (1962), and Pao and Mow (1973). In 1967 Miklowitz discussed the long-time solution for the response of the walls of a cavity excited by the passage of a compressional wavefront. He concluded that, following this excitation, energy would be retained on the cavity walls as circulating Rayleigh type waves which did not diminish in amplitude. These conclusions were later modified as it was recognised that circulating energy would be diminished by radiation damping. Papers by authors such as Baron and Parnes (1962), discussed the stress amplification effects on cavity walls in plane wave/cavity interactions and concluded that normal modes (eigensolutions), in particular the modes associated with P (compressional waves) and Rayleigh waves, were responsible for these effects. The literature concerned with

circulating elastic waves on cavity walls and underground openings is discussed in detail in Chapter 2.

It therefore occurred to the author that it should be possible to generate surface standing waves of a predominantly Rayleigh type on the walls of underground openings in rock with the use of a seismic source. A knowledge of the theoretical radial deformation modes at "resonance", when compared to the measured mode shapes in the field would then, in principle, provide a means of assessing the state of the rock mass surrounding the opening. Although there had been some discussion in the literature on the theoretical seismic radiation from a source on the wall of a cavity, none of these solutions were found to be of value in the calculation of the near-field (cavity-wall) response. Thus the initial objective was the development of a a new analytical solution.

From the analytical point of view the problem is essentially three dimensional if propagation down the axis of the tunnel is considered, but if the wavelengths generated are restricted to the order of the tunnel diameter, then a two dimensional or plane-strain analysis is justified. The analysis described in Chapter 3 begins with a description of a new solution method for evaluating the eigen-frequencies of the Viktorov frequency equation for cylindrical cavities in elastic media. This readily leads to a solution for the dynamic response of a cylindrical cavity of circular cross section within a linear elastic rock of infinite extent. Dynamic loading is in the form of a normal line source applied at one location on the cavity wall. Some discussion of the three-dimensional problem of a point source on a cavity wall is also included.

Analytically it is difficult to deal with openings of arbitrary cross-section, such as those frequently encountered in underground mines, other than by conformal mapping techniques. However, the dynamic Finite Element Method is a numerical solution technique which is gaining popularity for wave propagation studies and is ideally suited to arbitrary geometries. Thus, another major objective in this project was to establish the

accuracy of a Dynamic Finite Element simulation of the problem The DFEM method and applications to surface waves including the line source/cavity interaction are discussed in Chapter 4. Chapter 5 is devoted to comparisons between analytical and DFEM predictions. The "resonance" behaviour of cavities in infinite elastic media and the significance of the Viktorov poles are discussed in Chapter 6.

Experimental work was initiated at the Zinc Corporation Mine, Broken Hill, where a CSIRO, Division of Geomechanics, Rock Mechanics programme was in progress. The geophysical test developed involved seismic excitation in the audio frequency range of the walls of a tunnel (drive-way) with the use of a heavy duty electro-mechanical shaker. The response of the tunnel walls at various locations around the test circumference is then measured. Similar experiments, on a smaller scale, were conducted in a borehole within a large granite block in the laboratory.

It was necessary to develop a broad range of instrumentation for these experiments and a suite of computer programs for the analysis of the resulting data. Aspects of this work are described in Chapters 7 and 8.

Currently there is interest in the use of circumferentially propagating elastic waves for non-destructive testing applications. Uses include the measurement of stress induced anistropy around borehole walls via changes in circumferential propagation velocity. A circumferential device for remote logging of borehole fractures has been described by Setser (1981). Dowding (1978) has mentioned the possible role of circulating Rayleigh waves in damage to tunnel walls following surface explosions. There is also interest in the use of seismic sources, clamped to borehole walls to avoid unwanted resonances associated with tube-wave modes, for cross-hole tomographic mapping. Thus, the results presented in this thesis hopefully will be of use in the above applications and for geophysical and non-destructive testing applications involving circumferentially propagating elastic waves.

2. A literature review of the dynamic response of cavities in elastic media

When considering the dynamic response of cavities in elastic media it is useful to re-examine the physics of elastic surface waves, for as Pao and Mow (1976) state:

"An infinitely extended solid with a cylindrical cavity may also "oscillate". Because the medium is unbounded the free oscillations can only be expressed in the form of travelling waves".

An intuitive examination of the physics of the above problem suggests that these "free oscillations " will be confined to the vicinity of the cavity walls during steady-state oscillation and will therefore exist as a form of Rayleigh or surface waves circulating the cavity walls. In fact, Miklowitz (1980) refers to the problem of a line-source acting on the wall of a cavity of radius, a, located within an infinite elastic medium, as " basically a Lamb type problem for the exterior space r>a".

2.1 Surface waves on curved surfaces

Following the discovery of free elastic surface waves by Rayleigh (1885) subsequently termed "Rayleigh waves", Lamb (1904) published in the Philosophical Transactions of the Royal Society a mathematical treatise on the dynamic response of the surface of an elastic half space to various cases of force application. He considered several cases including harmonic line loads applied vertically, impulsive vertical line forces, horizontal forces, buried forces and the 3-dimensional case of a point force. The vertical impulsive line force is considered in greatest detail. Lamb (1904) showed that the surface application of an impulse of short duration results in the generation of a surface disturbance consisting of a "minor tremor" followed by the "main shock"---Figure 1. The minor tremor contains the first arrival consisting of longitudinal wave motion (P-wave), followed by the arrival of transverse wave motion (S-wave). The amplitude of these

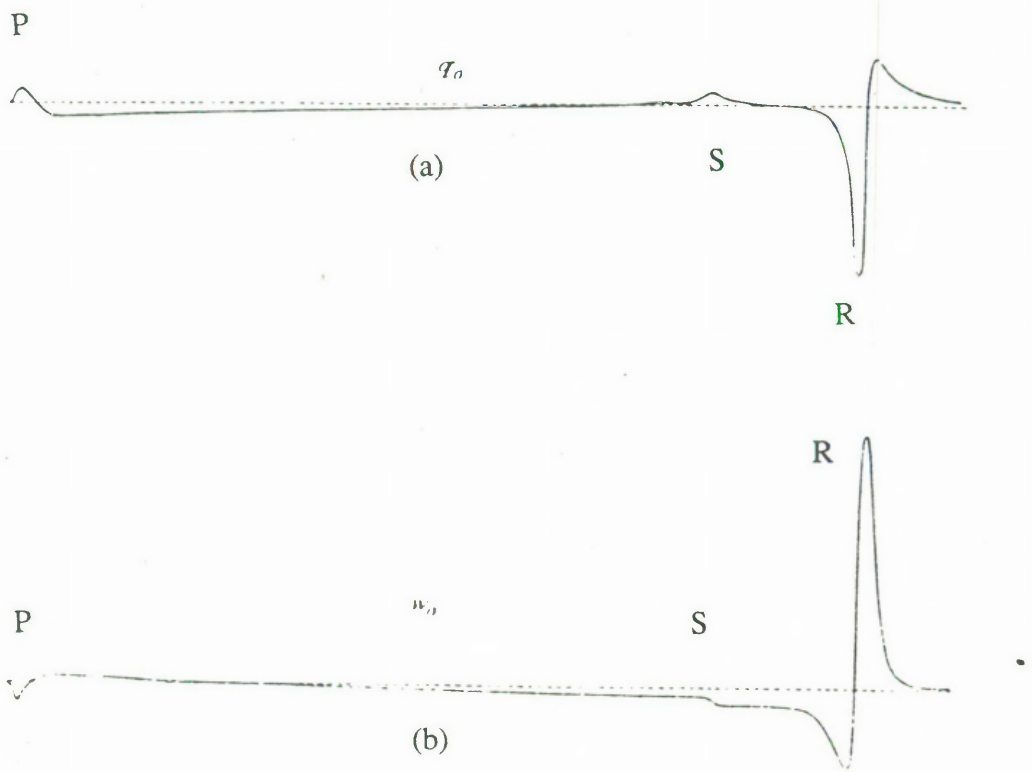

Figure 1. Horizontal (a) and vertical (b) displacement waveforms on the surface of an elastic medium at a large distance from a pulsed surface source -- after Lamb (1904). The compressional, shear and Rayleigh arrivals are denoted by P, S, and R respectively.

components is decreased and the time scale is increased with increasing distance from the source. In the 2-dimensional case the amplitude of the P and S components are to a first order approximation dependent on distance to the power -3/2.

In contrast, the main shock has an arrival time of that of Rayleigh waves (for a Poisson solid, the Rayleigh wave velocity is 0.9194 that of the shear wave velocity) and a constant time scale is preserved, i.e., propagation is not dispersive. The wave motion is largely confined to the surface and the particle motion is retrograde elliptical. In the 3-dimensional case its amplitude is decreased only by annular divergence (geometric spreading).

Lamb discusses the waveform of the Rayleigh component and notes that in the case of an impulsive source the waveform is that of a "solitary wave", i.e., it consists of one oscillation only. However, it is not sharpely defined in the rear as it is in front, but rather it has a prolonged tail which suggests it is a peculiarity of the 2-dimensional nature of the wavefront. In contrast, the 3-dimensional analysis suggests that the P and S components will be more clearly isolated than in the 2-dimensional case. In concluding his discussion, Lamb considers the propagation of similar disturbances over surfaces with curvature, such as the surface of the earth. He supports Oldham (1900) who had earlier suggested that in such cases there will be an increase in the minor tremor compared to the planar case due to the presence of a direct transmission path. The main shock, on surfaces with curvature, however, will still be caused by the Rayleigh waves travelling over the surface.

Sezawa (1927) considered the propagation of Rayleigh waves in the circumferential direction of a cylindrical surface, i.e., the inner surface of a hollow cylinder. He obtains a recursive relation involving Bessel functions whose arguments and orders are dimensionless wavenumbers. This equation is solved to give the dispersion relation between velocity and dimensionless radius of curvature. However, as this solution is

effectively concerned with circumferential propagation on the inner surface of a tube, it does not consider the added complexity of radiation into a surrounding medium.

Nakano (1928) discussed the particle motion of curved surfaces traversed by Rayleigh waves. He compares his solution to that of the Rayleigh solution for wave propagation on a planar surface where the particle motion is a retrograde ellipse with the excursion on the vertical axis being approximately twice that of the horizontal. Nakano notes that this is only true on curved surfaces for large distances from the origin and that in general the orientation of the major axis of the ellipse is dependent on distance from the source.

Cook and Valkenburg (1954) showed experimentally that Rayleigh waves at ultra-sonic frequencies may propagate on cylindrical surfaces and that they can traverse a curvature of radius of the order of a wavelength and larger.

Viktorov (1958) derived the frequency equation for the cases of surface wave propagation on both convex and concave surfaces. He discusses in detail the dispersive nature of the Rayleigh type propagation in the convex case and shows that similar dispersive behaviour occurs in the concave case. Viktorov's frequency equations are fundamental to any problem involving the dynamic behaviour of cavities in elastic media. They will be discussed in detail in chapter 3.

All discussions concerned with disturbances propagating on surfaces with curvature had concluded that the minor tremor (P and S components) will increase in amplitude with respect to the planar case. These arguments were concerned with convex surfaces such as the earth's surface. However, on concave surfaces such as the surface of boreholes it is suggested that the converse will be true, i.e the preceding P and S components in the wave train will be more effectively radiated into the surrounding medium and will be

consequently reduced in amplitude with respect to the planar case. They will also be reduced in amplitude with respect to the Rayleigh component.

2.2 Elastic wave/cavity interactions

The response of cylindrical cavities in infinite elastic media to various forms of axi-symmetric loading, e.g., pressure loading such as that generated in blasting, has been extensively discussed in the literature. Selberg (1952) considered the waveforms of stress waves emanating from both uniformly loaded spherical and cylindrical cavities in infinite elastic media (Poisson solids). In the cylindrical case the integral that is required to be evaluated for the radial stress-distance function involves a denominator which has only one complex root, namely,

$$-0.442057 + 0.447357i.$$

This root (allowing for sign convention changes) will be shown in later chapters to correspond to the n=0, P-wave branch of the cavity normal modes (given by solution of the Viktorov equation), i.e., the radially symmetric component of radiation only is involved. The tallies with Selberg's starting assumptions of a uniformly loaded cavity and short times such that no reflected energy is involved. Heelan (1953) considers the radiation of energy from a cylindrical cavity containing a cylindrical charge of finite length. The cavity walls are uniformly loaded. Thus, this paper appears to be an extension from Selberg's treatment of a cylindrical cavity of infinite length. However, there is some controversy concerning the validity of Heelan's boundary conditions (see Abo-Zena, 1977, for example).

In the late 1950's and throughout the 60's a great deal of attention was focused on the behaviour of underground structures such a tunnels and shelters when exposed to disturbances originating from surface blasts. This prompted many fundamental studies into elastic wave front interaction with cavities. Nishimura and Jimbo (1954) appear to have pre-empted this trend with a discussion of dynamical stress concentration factors

when spherical inclusions (both rigid inclusion and cavity are considered) are subjected to incident harmonic P-waves. They consider reflected and refracted waves at the cavity boundary. The refracted wave is treated as a standing wave on the cavity boundary. The authors conclude that the stress concentration at the cavity boundary exceeds the static case and is a maximum when 2π divided by the radiation wavelength is approximately 0.5.

The scattering of plane compressional and shear waves incident on a cylindrical discontinuity in an elastic solid was investigated by White (1958). A theoretical description of the mode conversions and directivity of the radiation scattered by the inclusion is backed up by an experimental investigation. Both empty and fluid-filled boreholes in aluminium are considered with the wavelength of the radiation being comparable to the borehole diameter.

The stresses around a cylindrical cavity in an elastic medium (Poisson solid) due to an incident step-function wavefront were examined by Baron and Matthews (1961). Stresses are derived by an integral transform approach. An expression for the singularities (poles) of the integrands for the stresses has a similar form to that of the Viktorov equation. However, Viktorov's equation is not mentioned. The stress amplification, particularly the hoop (circumferential) stresses, are considered to be due to the decay time-constant associated with the pole, 0.2862 + 0.2786i (this pole in fact corresponds to the n=2 normal-mode on the Rayleigh branch of the Viktorov equation roots). Baron and Parnes (1962) extend the previous paper (Baron and Mathews, 1961) to consider velocities and displacements.

A Fourier-Bessel series solution is described by Pao (1962) for the interaction of a plane compressional wavefront with a circular cavity in an elastic plate. Dynamic stress concentration factors 10% higher than the static values are calculated. The series solution for the cavity hoop stresses consists of Hankel function terms of similar form to the Viktorov equation although no reference is made to Viktorov. Pao (1962) states that for

the dimensionless wavenumber equal to 4, at least 16 terms are required for an accuracy of 1 part in 10^5. No mention of the significance of normal modes on the stress amplification effects are made. Pao and Mow (1962) extend Pao's (1962) paper to consider both fixed and movable rigid inclusions in the elastic plate. This work is followed by a further Fourier-Bessel solution by Mow and Mente (1963) for plane harmonic shear waves incident on a cavity (radius, a) in an infinite elastic medium. The case of a rigid inclusion is also considered. The response of the cavity for the dimensionless shear wavenumber, βa, in the range, $0.1<\beta a<3.0$ is considered for Poisson's ratio, 0.15, 0.25, and 0.35.

Miklowitz (1963) in his earlier studies of the line-load cavity interaction, had predicted that Rayleigh waves could exist on the cavity walls, following transient excitation, which were non-decaying in time and were independent of angular position (θ). In a later paper (Miklowitz, 1966) attention is focused on the plane compressional wave interaction with the cavity where Rayleigh waves are shown to exist on the cavity walls. They are still sizeable disturbances and predominate in the long-time solution. However, they are spatially attenuated with θ. The solution method is that of integral transforms where residues of the Viktorov poles provide the dominant contribution to the evaluation of the integrals. The full significance of the poles (roots of the Viktorov frequency equation) are discussed and it is shown that the Rayleigh contributions have the least damping. This work is described in detail by Miklowitz's research student, Peck, in his Ph.D dissertation (Peck, 1965).

Peralta et al. (1966) consider the solution described by Pao (1962) for the interaction of a plane compressional wavefront with a cavity and provide a simplifying approximation to the integrals to enable easy evaluation of the stresses. The resulting approximation matches the exact solution quite well and would be satisfactory for engineering purposes. However, the weakly oscillatory nature of the exact stress-wavenumber relation is lost. Cheng and Jananshahi (1967) discuss the dynamical stress concentration factors around a rigid circular inclusion and a cavity in an elastic plate excited by a line harmonic source at a

distance from the discontinuity, i.e., in contrast to previous work the incident wavefield is given by Lamb's solution for a line source in an infinite medium.

Peck and Miklowitz (1969) evaluate the " shadow zone " response, illustrated in Figure 2, of the diffraction of a compressional wavefront by a circular cavity. A "wave-sum" solution method is used in which the cavity response, as a function of θ, is represented by a sum of circumferentially propagating wave modes. This work shows that rapid convergence of the integrals is obtained in the shadow zone for step-function loading of the cavity. Only seven modes are required for an accurate solution. However, the solution is only applicable to the shadow zone. The authors note that the evaluation of the poles for this solution (roots of the Viktorov frequency equation) in the complex frequency plane presents many difficulties.

Pao and Mow (1973) provide a comprehensive review of the diffraction of elastic waves and the effects of dynamic loading on underground structures and openings. This work also contains a detailed analysis of the interaction of P and S waves with cavities. The latter chapters are essentially a re-iteration of Pao's and Mow's earlier publications However, there is included a discussion of the contribution of the poles of various transfer functions describing the cavity response.

Eason (1973) considered the radiation from spherical and cylindrical cavities in mildly anisotropic media following step-function loading of the cavity walls. A wavefront expansion method for calculating the stress field is used.

Pao and Sachse (1974) describe some experimental observations of the scattering, by a fluid filled hole in an aluminium block, of ultra-sonic pulses. The presence of strong resonance effects is noted. Sachse (1974) describes the experimental spectral analysis of wide-band ultra-sonic pulses scattered by a circular fluid-filled cavity in an aluminium block. Various fluids including air were considered. Similar work was reported by

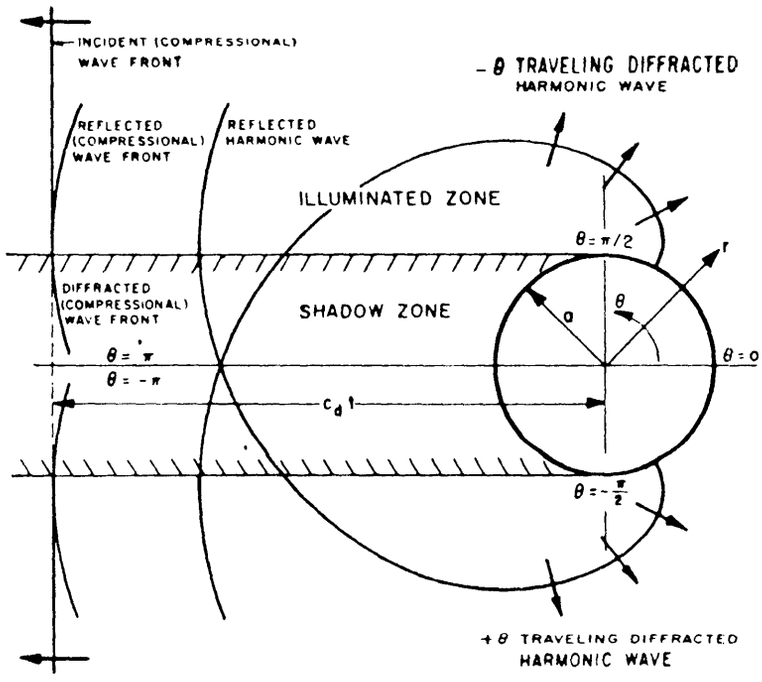

(a)

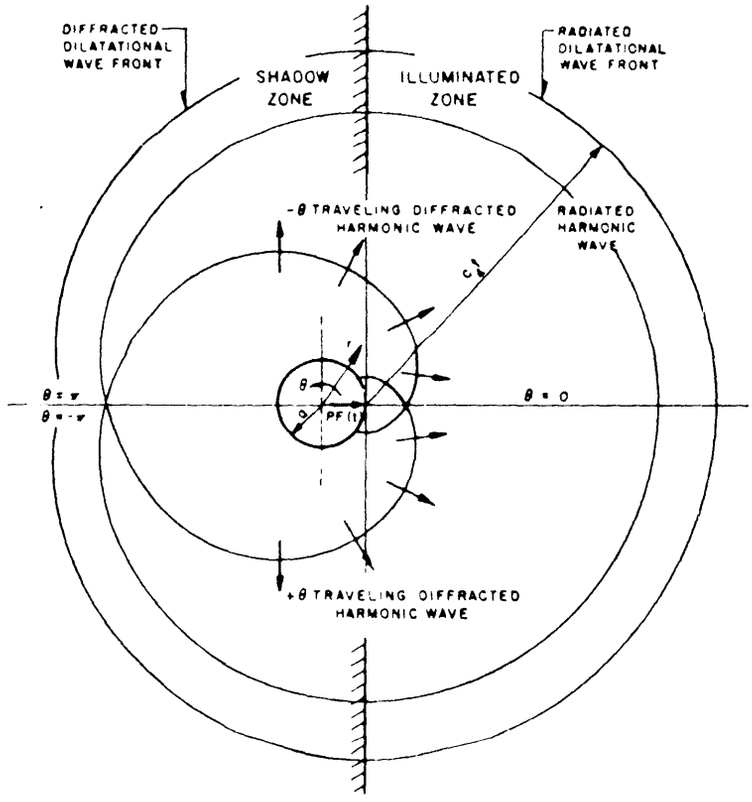

(b)

Figure 2.(a) Interaction of a compressional wavefront with a cylindrical cavity.

(b) Seismic radiation from a cylindrical cavity containing a source on the cavity wall -- after Miklowitz (1980).

Roever et al. (1974) who described the response in the radial, circumferential, and axial directions of a fluid filled borehole. The borehole fluid was excited by a sparker source lying on the borehole axis. The borehole wall response was not considered.

Glass (1974) reviewed seismic considerations in siting large underground openings in rock. His thesis is essentially a literature review of aspects of the diffraction of elastic waves by cavities in elastic media. The mathematical treatments of Pao and Mow (1973) and Miklowitz are reproduced in detail. Glass's own contribution is a numerical evaluation of some of the relevant expressions and a relatively simplistic (compared to the present investigation) dynamic finite element model. Eigenvalue and time-domain response solutions of single and multiple rectangular cavities are considered. He concludes that no resonant behaviour is observed in the numerical solutions for excitation frequencies in the range 1 - 100Hz.

Pao and Mow (1976) discuss the theory of normal modes (eigen-values) and their effects on the scattering of ultra-sonic pulses. The case treated in greatest detail is that of the fluid-filled cylindrical cavity in an elastic medium. However, the empty cavity is also considered as a limiting case.

Uberall (1977) points out the similarity of the Breit-Wigner resonance scattering formalism used in nuclear physics to that of the acoustic and elastic scattering. In both cases the interaction between the incident wave and the resonances of the scattering object determine the scattered wave amplitude. The author examines several cases in the light of this scattering theory including that of a water-filled cavity in an aluminium medium. He identifies various resonance peaks in the scattered wave field mainly due to fluid/cavity resonances. The empty cavity modes appear as a soft background, i.e., they are weakly excited in this case.

Buchwald (1978), in a mathematical note, considers the diffraction of elastic waves by small cylindrical cavities. This work amounts to an approximate solution to the Viktorov equations for small values of wavenumber via an asymptotic expansion of the Bessel functions involved. Greenfield (1978) derived the radiation pattern for the 3-dimensional case of a point source acting on a cavity. The method of formulation essentially follows the 2-dimensional case. However, a third wave-number is involved arising from the consideration of radiation down the axis of the cylindrical cavity. The scalar potentials thus involve a further integration over this wavenumber which has the effect of greatly increasing the difficulty of solution (in fact the solution is considered by some researchers to be analytically intractable). Greenfield applies a far-field approximation which has the effect of reducing the solution of the problem to that of the 2-dimensional case.

Miklowitz (1980) provides an excellent review of elastic wave interactions including his work and that of others in "Elastic Waves and Waveguides". In his chapter on scattering by cylindrical obstacles he discusses the scattering of an elastic pulse by a cylindrical cavity. A line source is considered acting at a distance from the cavity. Two limiting cases are considered; that of a line source on the cavity wall and that of a line source at infinity. The latter case corresponds to a plane wave travelling towards the cavity whereas the line source on the cavity wall, as Miklowitz states, is "basically a Lamb type problem for the interior space r>a". Miklowitz discusses integral transform methods of evaluating the cavity response with particular emphasis placed on the significance of the Viktorov poles, following Peck (1965). He restricts his analysis of the near-field case to that of the shadow-zone response and derives an integral expression for this case which is essentially a summation over the residues of the Viktorov poles. Miklowitz also considers the long-time, far-field solution in which the Rayleigh waves predominate since the limiting wavenumbers on the Rayleigh branch of the Viktorov equation are the only real wavenumbers in the spectrum. An approximate solution is derived for the circulating Rayleigh wave displacements. Similar methods, i.e., that of an asymptotic expansion

method, are applied by El-Akiliy and Datta (1980) to the analysis of the seismic response to buried pipes in an elastic medium.

Experimental observations of the interaction of longitudinal and transverse elastic waves with cylindrical cavities in a glass plate are described by Ying et al (1981). A strobed photoelastic technique is used to visualise the wavefront interactions. The authors discuss the presence of a "creeping wave " which travels from the illuminated side of the cavity to the shadow zone. The "creeping wave" is observed to radiate bulk waves into the surrounding medium as it progresses around the cavity loosing energy in the process --see Figure 3. The radiation process is accompanied by a phenomenon of "shooting successive tips". No doubt this "creeping wave "corresponds to a circulating Rayleigh wave first postulated by Miklowitz. However, the authors state that they are unaware of any analysis of interactions involving such a wave. In the longitudinal case the authors claim that the creeping wave velocity is approximately equal to the incident longitudinal-wave velocity whereas in the case of transverse-wave illumination the creeping wave has a velocity equal to 80% of the transverse wave velocity. The first observation is puzzling; however, in the latter case the creeping wave velocity is approximately equal to the expected value, i.e., that of Rayleigh waves.

Blair (1982) describes a dynamic finite element method (DFEM) analysis of the interaction of a step-function compressional wavefront with a cylindrical cavity. Good agreement is obtained with the results of Baron and Parnes (1962). The DFEM model is extended to include elastic inclusions, representative of seismic detector mounts, within the cavity. The amplitude transfer functions for the response of a seismic detector mounted on the walls of a borehole are discussed by Blair (1984) for the case of an incident compressional wavefront. The Fourier-Bessel series solution described by Pao and Mow(1973) is developed for this treatment and numerically evaluated for large dimensionless wavenumbers Cases considered include both fluid-filled boreholes and empty boreholes with wall mounted detectors.

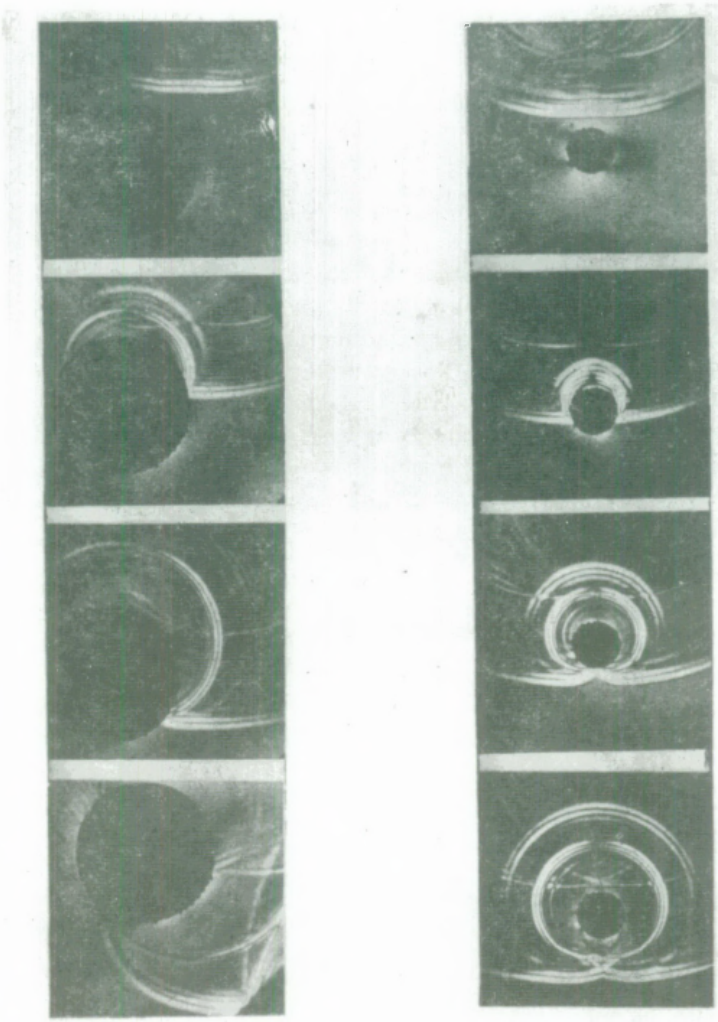

Figure 3. Direct observations of the interaction of a longitudinal wavefront with a cavity. A stroboscopic photoelastic technique was used -- after Ying et al. (1981)

The far-field displacement radiation patterns arising from a point source acting on the wall of a fluid-filled borehole are discussed by Lee (1986). The analysis considers only wavelengths large compared to the borehole diameter. This has the effect of restricting the normal-modes required to the 0th, 1st and 2nd orders.

2.2.1 Applications of seismic reciprocity to wave/cavity interactions

The principle of reciprocity states that a reciprocal relation holds between a point force and the resulting particle displacement at any two points respectively in an elastic medium. Knopoff and Gangi (1959) review the general principles of reciprocity in physics and apply these to the reciprocity between source and receiver in elastic wave propagation. The theoretical discussion is backed up by experimental observations. Thus, it should be possible to use reciprocity principles to deduce the far-field radiation pattern arising from a source within a borehole if the borehole response to an incoming plane wave is known. An application of reciprocity to calculate the far-field waveform arising from a localised force pulse within a borehole is discussed in Siggins and Stokes (1987) and in Chapter 5 of this dissertation. White (1960) applies seismic reciprocity principles to the derivation of the far-field particle displacement-distance relation for a pair of diametrically opposed forces acting on a borehole. He also considers, in a similar manner, the displacements in the far-field arising from a uniformly loaded borehole and shows how the use of reciprocity leads simply to the results of Heelan (1953). An experimental verification of reciprocity is demonstrated for the case of a hole in a plate. Similar conclusions concerning the use of reciprocity for the determination of far-field radiation patterns were reported by Gupta (1965).

Seismic reciprocity is invoked by Lee (1987) to compute the borehole wall displacements, arising from an incoming plane wave, from his earlier solution. Again the analysis is restricted to wavelengths larger than the borehole diameter.

2.3 Non-destructive testing applications of circumferentially propagating waves.

Little use has been made of the circumferential propagation of elastic waves as yet for geophysical and non-destructive testing, possibly because of the complexity of the

analyses required. However, Vogel and Herolz (1981) have described a borehole logging tool which propagates several wave modes around the walls of a fluid filled borehole. The largest amplitude wave is thought by the authors to be a circumferentially propagating guided fluid wave. The amplitude of an additional wave, the "refracted shear wave", is shown experimentally to be sensitive to the presence of cracks in the borehole walls.

Su et al. (1983) describe the experimental measurement of the stress field around a borehole in a sandstone block using ultra-sonic transducers. The transducers, a transmitter and a receiver, are clamped within a borehole in a sandstone block. Velocities of first arrivals propagating from the transmitter to the receiver, over a small arc of the borehole circumference, are measured. The authors make the assumption that all wave modes generated will be compressional. This is justified by an argument using the radiation pattern of a "piston-source" in which the compressional-mode lobe of the radiation pattern is extended by a suitable choice of wavelength and transmitter diameter to reach the receiver element. However, it is debatable whether or not the piston source (a well known representation of an acoustic source in air such as a loud-speaker) is truly representative of what amounts to a Lamb type problem on a surface with curvature and possessing a finite shear modulus. The data were obtained by first testing the cores taken from the sandstone blocks to obtain a stress-velocity calibration function. The biaxially loaded blocks were then tested by measuring velocities in increments around the inner circumference of the boreholes. Angular separation between transducers was 36 degrees. Velocities measurements were made every 30 degrees with the transducers being rotated from the origin in 30 degree steps. In that manner it was claimed that the stress distribution around the borehole was obtained. However, a suprisingly high stress-velocity sensitivity was reported. The work of Su et al. (1983) represents an interesting application of the use of circumferential propagation of elastic waves and would possibly benefit from the results presented in this dissertation.

3. Theoretical analysis

3.1 Nomenclature

Φ, Ψ, X	elastic wave displacement potentials.
$\bar{\Phi}, \bar{\Psi}, \bar{X}$	" "
a	cavity radius (m)
ω	circular frequency, radians per second (equal to $2\pi f$, where f is frequency in Hz)
k_1	dilatational wavenumber (m^{-1})
k_2	shear wave number (")
k_3	Rayleigh wavenumber (")
k	generalised wavenumber (")
C_D	dilatational wave phase-velocity (m/s)
C_S	shear wave phase-velocity (")
C_R	Rayleigh wave phase velocity (")
ρ	density, kg m^{-3}
λ, μ	Lame elastic constants (Pa)
E	Young's modulus (Pa)
ν	Poisson's ratio
u_r, u_θ, u_z	displacement components in cylindrical polar coordinates (m)
$\sigma_{rr}, \sigma_{r\theta}, \sigma_{rz}$	stresses " " (Pa)
J_n	Bessel function of order, n.
H_n	Hankel function of order n.(equal to J + iY, where Y is a Bessel function of the second kind)
δ	Dirac delta function.
x,y	dimensionless wavenumbers equal to k_1a and k_2a respectively
x,y	dimensionless wavenumbers equal to $(k^2 - k_1^2)^{1/2}a$ and $(k^2 - k_2^2)^{1/2}a$ respectively.

3.2 The frequency equation for cylindrical cavities in elastic media

The geometry of the problem is defined by Figure 4. The discussion is limited to the plane-strain case. Thus, when the problem is defined in cylindrical coordinates, r, θ and z, the z dependence can be ignored. The solution procedure consists of expressing the displacement potentials, Φ, and Ψ, arising in the elastic wave equations, in terms of a Fourier-Bessel expansion. Stresses are derived from the potentials and boundary conditions are applied resulting in the desired solution.

The wave equations for an elastic continuum are

$$\nabla^2 \Phi + k_1^2 \Phi = 0$$
$$\nabla^2 \Psi + k_2^2 \Psi = 0 \qquad \text{---(1)}$$

where the operator, ∇^2 is given by

$$\nabla^2 = \frac{1}{r}\frac{\partial}{\partial r}\left(r\frac{\partial}{\partial r}\right) + \frac{1}{r^2}\frac{\partial^2}{\partial \theta^2}$$

The potentials, Φ and Ψ, apply to dilatational (longitudinal) and distortional (transverse) waves respectively. The wavenumbers k_1 and k_2 are given by,

$$k_1 = \omega/C_D \text{ and } k_2 = \omega/C_S$$

where ω is the circular frequency and C_D and C_S are the dilatational and shear wave phase velocities respectively. Phase velocities are given by

$$C_D = \left(\frac{\lambda + 2\mu}{\rho}\right)^{1/2} \qquad \text{---(2)}$$

$$C_S = \left(\frac{\mu}{\rho}\right)^{1/2}$$

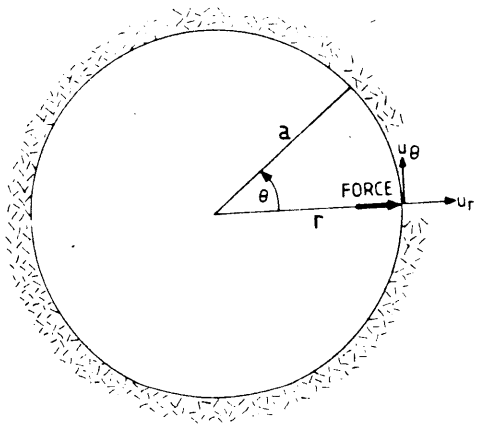

Figure 4. Geometry of the line-force/ cavity interaction.

where λ and μ are Lame' elastic constants.

The radial displacement, u_r, and the tangential displacement, u_θ, are given by,

$$u_r = \frac{\partial \Phi}{\partial r} + \frac{1}{r}\frac{\partial \Psi}{\partial \theta} \qquad ---(3)$$

$$u_\theta = \frac{\partial \Phi}{r\partial \theta} - \frac{\partial \Psi}{\partial r} \qquad ---(4)$$

The corresponding stresses are given by

$$\sigma_{rr} = \frac{\lambda}{C_D^2}\frac{\partial^2 \Phi}{\partial t^2} + 2\mu\left[\frac{\partial^2 \Phi}{\partial r^2} + \frac{\partial}{\partial r}\left(\frac{1}{r}\frac{\partial \Psi}{\partial \theta}\right)\right] \qquad ---(5)$$

$$\sigma_{r\theta} = \mu\left[\frac{1}{C_S^2}\frac{\partial^2 \Psi}{\partial t^2} + 2\left(\frac{\partial^2 \Phi}{r\partial r\partial \theta} - \frac{\partial \Phi}{r^2\partial \theta} - \frac{\partial^2 \Psi}{\partial r^2}\right)\right] \qquad ---(6)$$

The wave equations, (1) in cylindrical coordinates, are in the form of Bessel's differential equations and thus have Bessel function solutions. Viktorov (1958) makes the assumption that a generalised Rayleigh wave will exist on a curved surface. Thus the solution will be a function of $e^{ip\theta}$ where i has its usual meaning ($i^2 = -1$) and p is a dimensionless quantity which Viktorov terms an "angular wavenumber". It should be noted that, in general, p does not have to be restricted to integer values, but in Viktorov's treatment p is integer.

Thus, the solutions sought for propagation on a surface with curvature will be in the form

$$\Phi = A\, e^{ip\theta} J_p(k_1 r) \qquad ---(7)$$

$$\Psi = B\, e^{ip\theta} J_p(k_2 r) \qquad ---(8)$$

where A and B are arbitrary constants. $J_p(k_1 r)$ and $J_p(k_2 r)$ are Bessel functions of order p. However, these solutions do not satisfy the requirement of radiation into the

surrounding medium, i.e., they are only applicable for the case of surface wave propagation on the surface of a cylinder. In the case of a cavity the solutions required are

$$\Phi = Ae^{ip\theta}H_p^{(1)}(k_1 r) \qquad \text{---(9)}$$

$$\Psi = Be^{ip\theta}H_p^{(1)}(k_2 r) \qquad \text{---(10)}$$

where $H^{(1)}_p$ are Hankel functions of the first kind which are defined in terms of the Bessel functions of the first kind and second kinds , J and Y respectively, as,

$$H^{(1)} = J + iY$$

(refer Abramovitz and Stegun, 1965).

The Hankel functions for r > a represent cylindrical waves travelling out along the radius. The time dependence for the displacement fields is $e^{-i\omega t}$.

The boundary conditions for the problem are zero stresses, σ_{rr} and $\sigma_{r\theta}$, at the cavity boundary, at r=a. The appropriate differentiations of expressions (9) and (10) are then substituted into (5) and (6). Applying the boundary conditions and making use of the recursion relations

$$H_{p-1}(x) + H_{p+1}(x) = \frac{2p}{x}H_p \qquad \text{---(11)}$$

$$H'_p(x) = \frac{1}{2}\left[H_{p-1}(x) - H_{p+1}(x)\right] \qquad \text{---(12)}$$

where x is the argument of the Hankel functions of order p and H'_p signifies the derivative of H_p with respect to argument, leads to Viktorov's frequency equation in the form of the recursion relation

$$\frac{H_{p+2} + H_{p-2}(x) - 2(y^2/x^2 - 1)\, H_p\ (x)}{H_{p+2}(x) - H_{p-2}(x)} = \frac{H_{p+2}(y) - H_{p-2}(y)}{H_{p+2}(y) + H_{p-2}(y)} \qquad ---(13)$$

(Note that the superscript, $^{(1)}$, has been dropped to avoid confusion with the derivative in later expressions).

The arguments x and y are the dimensionless wave-numbers, k_1a and k_2a, respectively. In terms of the Lame' constants, x is given by $\omega a(\rho/(\lambda + 2\mu))^{1/2}$ and y is given by $\omega a(\rho/\mu)^{1/2}$, where ρ is density.

Viktorov (1958) does not attempt to evaluate the zeros of (13), but makes the observation that, for real x and y, p will be complex. He applies an asymptotic expansion for the Bessel functions and concludes that, in an analogous manner to the convex case, circumferential propagation of elastic waves on a cavity will be dispersive.

As is shown by Stokes and Siggins (1987) the complex zeros of equation (13) are common to a number of transfer functions described in the literature. For, example Pao and Mow (1973) derive a Fourier-Bessel series for the cavity hoop-stress response to an incoming plane compressional wave. The transfer function for this case is also discussed in detail by Blair (1984).

With a change of notation its p^{th} coefficient has a denominator, D_p, given by,

$$\begin{aligned} D_p = {} & xH_{p-1}(x)\left[(p^2 - 1)yH_{p-1}(y) - (p^3 - p + y^2/2)H_p(y) \right] \\ & -H_p(x)\left[(p^3 - p + y^2/2)yH_{p-1}(y) - (p^2 + p - y^2/4)y^2H_p(y) \right] \end{aligned} \qquad ---(14)$$

(There appears to be an error in Pao and Mow (1973) in that y^2 in the last term of (14) is omitted).

By using the recurrence relations (11) and (12) it is possible to reduce (14) to the form

$$D_p = (p^2 - 1)xyH_p'(x)H_p'(y) - \frac{y^2}{2}[xH_p'(x)H_p(y) + yH_p'(y)H_p(x)] + \left[p^2 - (p^2 - \frac{y^2}{2})^2\right]H_p(x)H_p(y) \qquad ---(15)$$

Viktorov's equation, V_p, defined as

$$V_p = \frac{H_{p+2}(x) + H_{p-2}(x) - 2(y^2/x^2 - 1)H_p(x)}{H_{p+2}(x) - H_{p-2}(x)} - \frac{H_{p+2}(y) - H_{p-2}(y)}{H_{p+2}(y) + H_{p-2}(y)} = 0 \qquad ---(16)$$

can then be shown (Stokes and Siggins, 1987) to be given by,

$$V_p = \frac{-8D_p}{x^2y^2[H_{p+2}(x) - H_{p-2}(x)][H_{p+2}(y) + H_{p-2}(y)]} = 0 \qquad ---(17)$$

Since Hankel functions have no singularites, except at x = y = 0, the zeros of V_p are those of D_p. Stokes and Siggins (1987) show that other transfer functions, such as that described by Miklowitz (1980) for the cavity response to a line-source within an elastic medium, have the same poles (zeros of the denominator).

Dividing D_p by $H_p(x)H_p(y)$ yields

$$(p^2 - 1)F(x)F(y) - y^2/2[F(x) + F(y)] + p^2 - (p^2 - y^2/2)^2 = 0 \qquad ---(18)$$

where $F(x) = xH_p'(x)/H_p(x)$.

The Hankel function ratios, F(x), can be conveniently computed by the use of continued fraction expansions. The expansion is derived from the recurrence relation for the confluent hypergeometric function (Abramovitz and Stegun,1965, 13.4.15). The theory is set out by Temme (1975), but in the present case is simpler because a normalising sum is not required. Then

$$F(x) = ix - 1/2 + \cfrac{p - 1/4}{2 - 2ix - \cfrac{(p - 9/4)}{4 - 2ix - \cfrac{(p - 25/4)}{6 - 2ix...}}} \qquad ---(19)$$

3.2.1 Calculation of the Viktorov poles.

Expression (18) is analytic in both p and x (and hence y). Consequently the equation implicitly determines either p as a function of x or vice-versa, and that function is generally multi-valued and analytic except at branch points. For physical considerations discussed later in this dissertation it is convenient to hold p real and consider poles in the complex plane of x (and y). However, other authors, such as Miklowitz (1980), constrain x to be real and examine poles in the complex p-plane. Table 1 gives a comparison of some poles calculated by the above method with others in the literature for Poisson's ratio, ν, equal to 0.25 ($\nu = \lambda/2(\lambda + \mu)$).

Being an expansion for large argument, equation (18) seems to avoid the numerical difficulties encountered by other authors for increasing p. Convergence difficulties arise only when x closely approaches the negative imaginery axis. Continuous trajectories of the poles in the complex x-plane were calculated using a modified Newton-Raphson method for positive p up to p = 10 (Appendix 1 lists a Fortran programme, NIKZX for this purpose). These are shown in Figure 5. As noted in Pao and Mow (1973), for positive integer values of p = n, there are n poles if n is odd and n + 1 poles if n is even. All but one of the trajectories approach the imaginary axis as p diminishes, cross at p = 2n - 1/2, then continue as a mirror image reflected about the imaginary axis. The exception is a single trajectory which reaches p = 0; since (18) is an even function of p, the trajectory here meets its negative p counterpart at a branch point.

The p-values are marked on the trajectories where p is an integer. The trajectories are plotted as far as p = 10. Asymptotically the behaviour of the various branches is as described by Peck and Miklowitz (1969) with x regarded as the independent variable rather than p. Most of the poles arise when either $H_p(x)$ or $H_p(y)$ enter the transition region for Bessel functions where the argument is approximately equal to the order, and an expansion for the Bessel function in terms of the Airy function applies. For $p \cong x$, then,

$$x \cong p - a_j (p/2)^{1/3} w \qquad j = 1,2,... \qquad \text{---(20)}$$

p	Our value	Pao and Mow, 1973	Baron and Parnes, 1962
0	0.4474 - 0.4420 i	0.44647 - 0.44127 i	0.4464 - 0.4410 i
1	1.09272 - 0.7653 i	1.09272 - 0.7653 i	1.0929 - 0.441 i
2	1.90754 - 0.8978 i	1.90754 - 0.8978 i	1.9076 - 0.897 i
3	2.75652 - 0.9915 i	2.75652 - 0.9915 i	
4	3.63132 - 1.0666 i	3.63132 - 1.0666 i	
5	4.52440 - 1.1314 i	4.52440 - 1.1314 i	

Table 1. Comparison of calculated eigenvalues for circular cavities in elastic media. Poisson's ratio = 0.25.

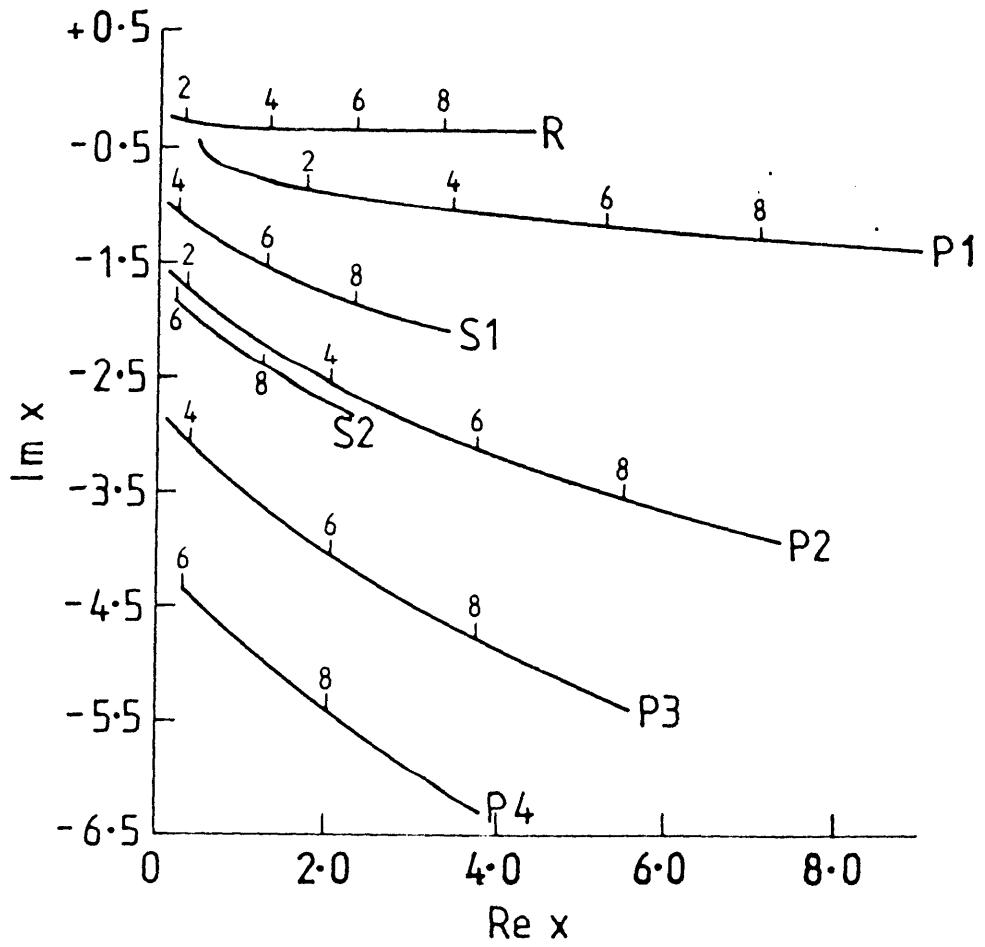

Figure 5. Locii of poles in the complex x-plane. R, P, S indicate Rayleigh, compressional and shear wave modes respectively. Integer values of p are marked on pole trajectories.

Table 2.

p	x value at zero of D		Derivative	
	Real	Imag	Real	Imag
		P1 branch		
0.000	0.4474	-0.4420	-0.4999	-0.2448
1.000	1.0927	-0.7654	-4.9668	7.4510
2.000	1.9075	-0.8978	-30.0801	36.8774
3.000	2.7565	-0.9915	-99.0362	105.8696
4.000	3.6313	-1.0666	-241.8189	235.9453
5.000	4.5244	-1.1314	-492.8187	451.8991
6.000	5.4306	-1.1899	-889.7499	781.5193
7.000	6.3467	-1.2440	-1473.0596	1255.3524
8.000	7.2702	-1.2950	-2285.5579	1906.5410
9.000	8.1998	-1.3435	-3372.2041	2770.6892
10.000	9.1342	-1.3900	-4779.8574	3885.7664
		R branch		
2.000	0.2862	-0.2786	-4.9601	1.4331
3.000	0.7946	-0.3245	-26.0566	-6.9026
4.000	1.2979	-0.3437	-71.0670	-30.3484
5.000	1.8027	-0.3525	-151.0883	-74.4564
6.000	2.3098	-0.3559	-278.2668	-144.4714
7.000	2.8192	-0.3560	-465.3952	-245.1723
8.000	3.3307	-0.3542	-725.7965	-380.8448
9.000	3.8440	-0.3510	-1073.1565	-555.3453
10.000	4.3588	-0.3469	-1521.5138	-772.0622
		P2 branch		
2.000	0.4041	-1.7852	64.5148	-77.1535
3.000	1.2325	-2.2281	381.3022	-23.6993
4.000	2.0782	-2.5798	874.4141	395.4999
5.000	2.9359	-2.8760	1414.0438	1339.6630
6.000	3.8033	-3.1336	1860.6656	2926.2717
7.000	4.6787	-3.3625	2074.7217	5252.8540
8.000	5.5612	-3.5692	1917.3248	8407.5664
9.000	6.4501	-3.7580	1249.5570	12474.1729
10.000	7.3446	-3.9322	-68.2529	17534.6934

Table 2 (continued).

S1 branch

4.000	0.2580	-1.1025	-85.9125	193.4471
5.000	0.7711	-1.3573	-428.2726	306.4424
6.000	1.2858	-1.5530	-1015.4634	306.9080
7.000	1.8036	-1.7144	-1868.3984	129.3510
8.000	2.3246	-1.8528	-3012.7083	-288.1648
9.000	2.8486	-1.9745	-4474.5874	-1009.1045
10.000	3.3752	-2.0835	-6279.9517	-2099.0527
p	x value at zero of D		Derivative	

P3 branch

4.000	0.4155	-3.1005	496.9440	-1230.6393
5.000	1.2554	-3.6245	2376.0454	-1691.7261
6.000	2.1053	-4.0664	5293.3813	-1130.9962
7.000	2.9635	-4.4518	8977.6406	911.3301
8.000	3.8289	-4.7958	13116.4980	4775.0220
9.000	4.7005	-5.1076	17393.8184	10721.2168
10.000	5.5777	-5.3938	21501.0898	18962.2012

S2 branch

6.000	0.2542	-1.8734	-321.9348	1263.5731
7.000	0.7625	-2.1746	-1445.1500	1955.0776
8.000	1.2721	-2.4264	-3231.8972	2488.4888
9.000	1.7840	-2.6448	-5729.9917	2727.8069
10.000	2.2983	-2.8387	-8987.1289	2553.8904

P4 branch

6.000	0.4199	-4.4230	1669.4871	-6051.8496
7.000	1.2660	-4.9842	7091.9971	-8432.7812
8.000	2.1185	-5.4749	15154.9092	-8953.7119
9.000	2.9771	-5.9140	25458.0840	-6767.7256
10.000	3.8410	-6.3131	37521.6367	-1206.1699

Table 2. Table of zeros of $D_p(x)$ for small integer p, and complex x. The derivatives of D with respect to x at the zeros are also given; these are needed in calculating residues.

where $w = \exp(-2\pi i/3)$ and a_j is the j^{th} zero of the Airy function, Ai.

The phase velocity approaches that for P-waves, and the trajectories are labelled P1,P2,...

Similarly there are trajectories for which

$$y \cong p - a_j (p/2)^{1/3} w \qquad j = 1,2,... \qquad \text{---(21)}$$

These have phase velocities approaching that for S-waves and are labelled S1,S2,...

Finally there is a pole which is obtained from the Debye expansion for H(x) where $|x|,|y| < |p|$. This is the Rayleigh wave pole,with

$$x \cong (C_R/C_D)p + \text{constant} \qquad \text{---(22)}$$

where C_R is the phase velocity for Rayleigh waves.

Table 2 presents zeros for integer values of p, together with derivatives of D_p with respect to x. These are needed in order to calculate the residues, if the integral arising from the use of a Fourier-Bessel series as a transfer function is to be evaluated by residue calculus.

3.3 A line-source on a cavity wall

The analytical treatment of this problem follows similar lines to that of the cavity frequency-equation treatment in that Fourier-Bessel methods are employed. The method used is similar to that of of Pao and Mow (1973) for incident wave problems and Miklowitz (1980), but a more elegant solution is arrived at.

The geometry of the line-source/cavity interaction is summarised in Figure 4. Applying separation of variables, solutions of the following form are sought,

$$\Phi = \sum_{n=-\infty}^{\infty} \alpha_n H_n(k_1 r)\, e^{in\theta} \qquad \text{---(23)}$$

$$\Psi = \sum_{n=-\infty}^{\infty} \beta_n H_n(k_2 r)\, e^{in\theta} \qquad \text{---(24)}$$

where α_n and β_n are the Fourier coefficients.

As in the previous treatment, Hankel functions of the first kind, $H^{(1)}_n$, arise as a result of radiation away from the cavity walls. The time variation of the displacement field is given by $e^{-i\omega t}$ and has been omitted from (23) and (24).

The line-load will produce a normal stress at r = a which can be represented by a Dirac delta-function, $\delta(\theta)$ at $\theta = 0$, as is illustrated in Figure 4. The stresses σ_{rr} and $\sigma_{r\theta}$ can be represented by ,

$$\sigma_{rr} = \sum_{n=-\infty}^{\infty} \sigma_{rr_n} e^{in\theta} \qquad \text{---(25)}$$

and

$$\sigma_{r\theta} = 0. \qquad \text{---(26)}$$

Hence for each n, stress $\sigma_{rr_n} = 1$, since,

$$\delta(\theta) = \sum_{n=-\infty}^{\infty} e^{in\theta}$$

This enables α_n and β_n to be determined by equating coefficients, i.e, the appropriate differentiations of the potentials, (23) and (24), are substituted into the equations for the stresses, (5) and (6), and the boundary conditions, (25) and (26) are applied. This yields,

$$2\mu \begin{bmatrix} \frac{-\lambda}{2\mu} x^2 H_n(x) - x H_n'(x) + (n^2 - x^2) H_n(x) & in[\, y H_n'(y) - H_n(y)] \\ in[\, x H_n'(x) - H_n(x)] & (\frac{y^2}{2} - n^2)\, H_n(y) + y H_n'(y) \end{bmatrix} \begin{bmatrix} \alpha_n \\ \beta_n \end{bmatrix} = \begin{bmatrix} a^2 \\ 0 \end{bmatrix}$$

---(27)

Solving for α_n and β_n gives

$$\begin{bmatrix} \alpha_n \\ \beta_n \end{bmatrix} = \frac{a^2}{2\mu D_n} \begin{bmatrix} (\frac{y^2}{2} - n^2)\, H_n(y) + y\, H_n'(y) \\ in[H_n(x) - x H_n'(x)] \end{bmatrix} \qquad \text{---(28)}$$

Where D_n, is the determinant of the square matrix in (27) and is given by,

$$D_n = xy\,(n^2 - 1)H_n'(x)\,H_n'(y) - \frac{y^2}{2}\left[xH_n'(x)H_n(y) + yH_n'(y)H_n(x)\right] + \left[n^2 - (n^2 - \frac{y^2}{2})^2\right]H_n(x)H_n(y) \qquad ---(29)$$

Thus, when n is replaced by p, equation (29) can be seen to be identical to equation (15) and consequently the zeros of (15), i.e., the Viktorov poles, will determine the poles of the transfer function for the line-source on the cavity wall.

A series solution for the radial displacement, u_r, is obtained in the following manner:

The expressions for the coefficients, (28), are substituted into (23) and (24) and the appropriate derivatives into the equation for the radial displacement, (3). A similar process can be followed for u_θ; however, the discussion at this stage is confined to the radial displacement.

u_r is then given by

$$u_r = e^{-i\omega t}\sum_{n=-\infty}^{\infty} e^{in\theta}\left[\alpha_n k_1 H_n'(k_1 r) + \frac{in}{r}\beta_n H_n(k_2 r)\right] \qquad ---(30)$$

Then at $r = a$

$$u_r = e^{-i\omega t}\sum_{n=-\infty}^{\infty} e^{in\theta}\frac{a}{2\mu D_n}\left[xyH_n'(x)\,H_n'(y) + \frac{y^2}{2}xH_n'(x)H_n(y) - n^2 H_n(x)H_n(y)\right]. \qquad ---(31)$$

Hence ,

$$u_r = e^{-i\omega t}\sum_{n=-\infty}^{\infty} e^{in\theta}\frac{a}{2\mu}\,N_n/D_n \qquad ---(32)$$

where

$$N_n = F_n(x)\,F_n(y) + (y^2/2)\,F_n(x) - n^2, \qquad ---(33)$$

and

$$D_n = (n^2 - 1)F_n(x)F_n(y) - (y^2/2)\left[F_n(x) + F_n(y)\right]$$

$$+ n^2 - (n^2 - y^2/2)^2 \qquad \text{---(34)}$$

F(x) is defined, as in the previous case, as $xH'_n(x)/H_n(x)$.

It is convenient to carry out the summation for u_r in the complex x-plane using the continued fractions expansion (19) for the Hankel function ratio, $F_n(x)$. The summation is dominated by the Viktorov poles associated with the denominator, D_n. The series for u_r is convergent in θ except for θ approaching zero since its terms tend to $e^{in\theta}/|n|$. However, (32) can be made to converge at $\theta = 0$ by subtracting the following expression,

$$\frac{a}{2\mu(x^2/y^2 - 1)} \sum_{n=-\infty}^{\infty'} \frac{e^{in\theta}}{|n|},$$

where the prime denotes that the summation excludes the n = 0 term.

The series,

$$\sum_{n=-\infty}^{\infty'} \frac{e^{in\theta}}{|n|}$$

is equal to $\ln[2(1 - \cos\theta)]$. Thus, this process is equivalent to subtracting a Lamb (1904) type singularity, which has similar logarithmic properties, at the source and ignoring the radially symmetric component of the radiation. Implications of this step will be discussed in later chapters.

The series for u_r, (32), was summed to convergence for selected values of θ and for small increments of k_1a [Re (x)] in the range $0.05 \leq k_1a \leq 5.0$. Appendix 1 lists a computer program, LLD2, for this purpose. Figure 6 presents the convergence behaviour of (32). Convergence is achieved to an accuracy of 5 significant figures with 30 terms in the above range. The results are presented in Figures 7 to 10. Since the complex displacements (amplitude and phase) are effectively normalised by the applied stress these plots are equivalent to the compliance transfer functions of the cavity.

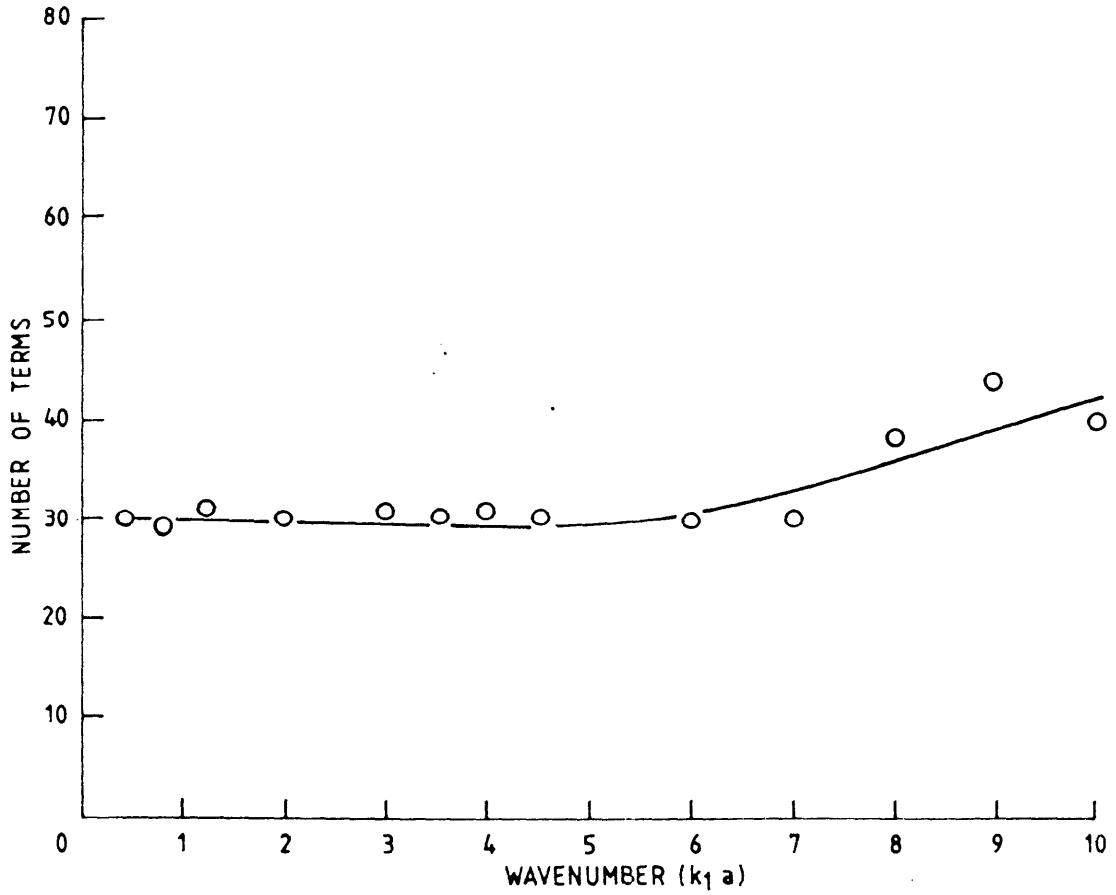

Figure 6. Convergence behaviour of the Fourier-Bessel series solution (32)

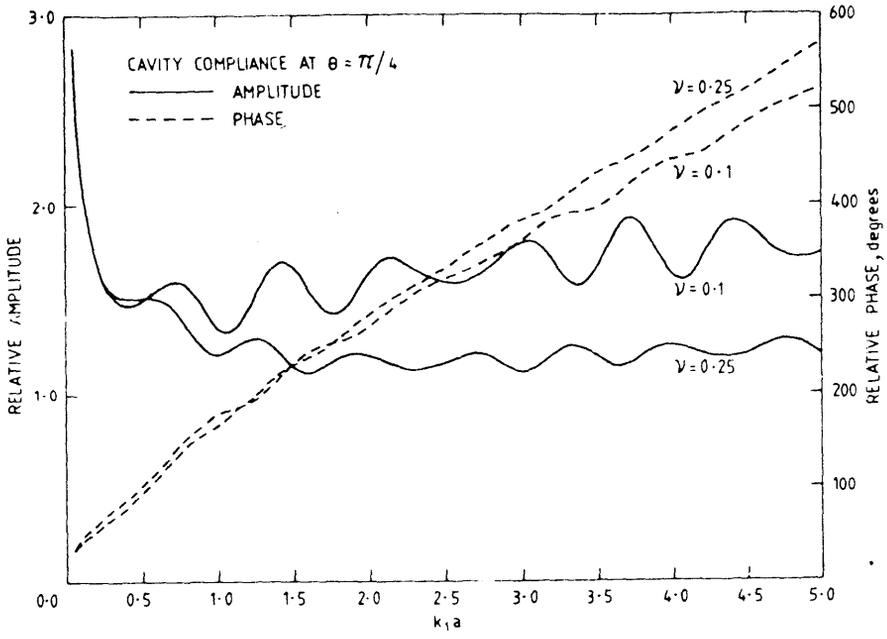

(a)

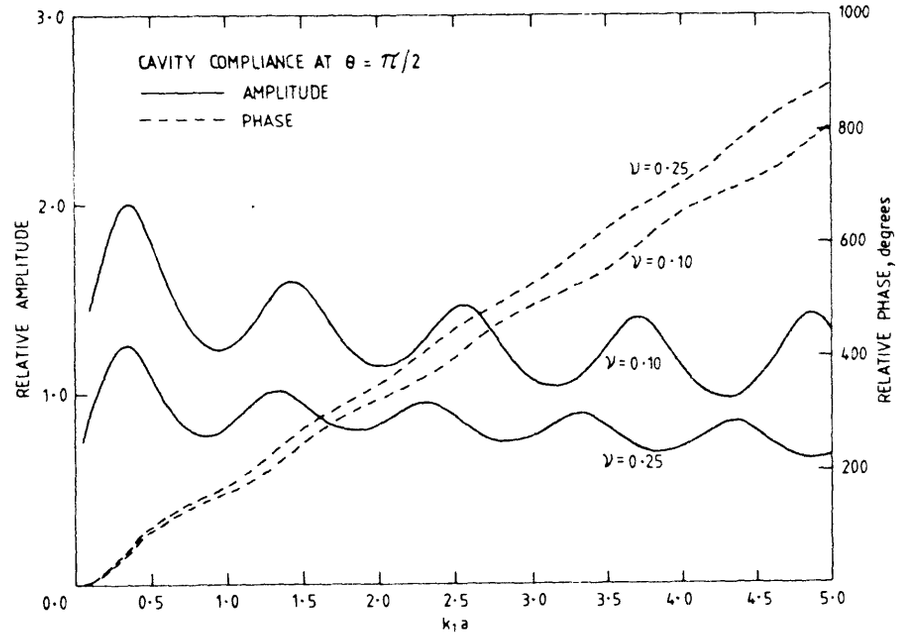

(b)

Figure 7. Compliance transfer functions (output displacement/input force) for the cavity wall at; (a) $\theta = \pi/4$, (b) $\theta = \pi/2$. The source is at the origin.

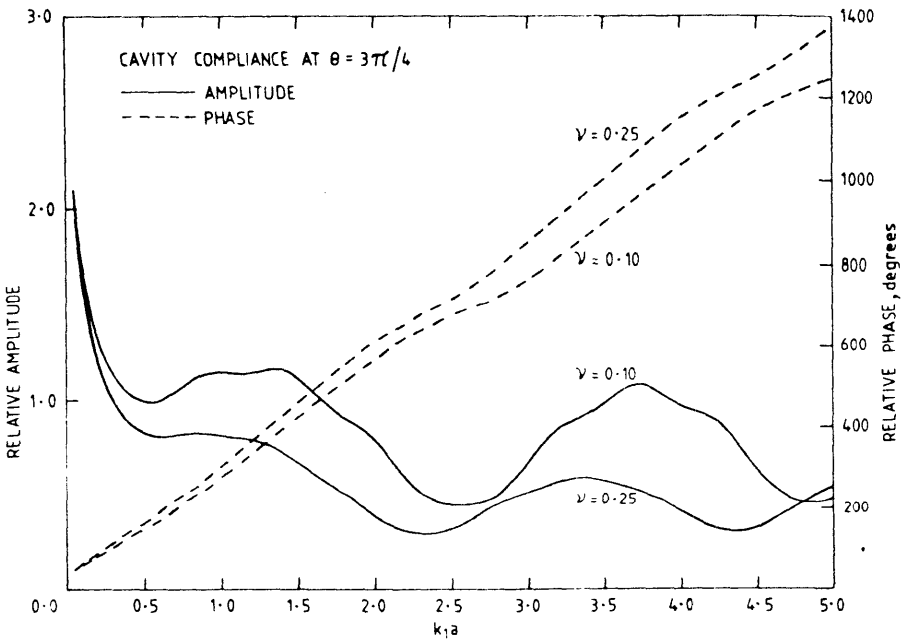

(c)

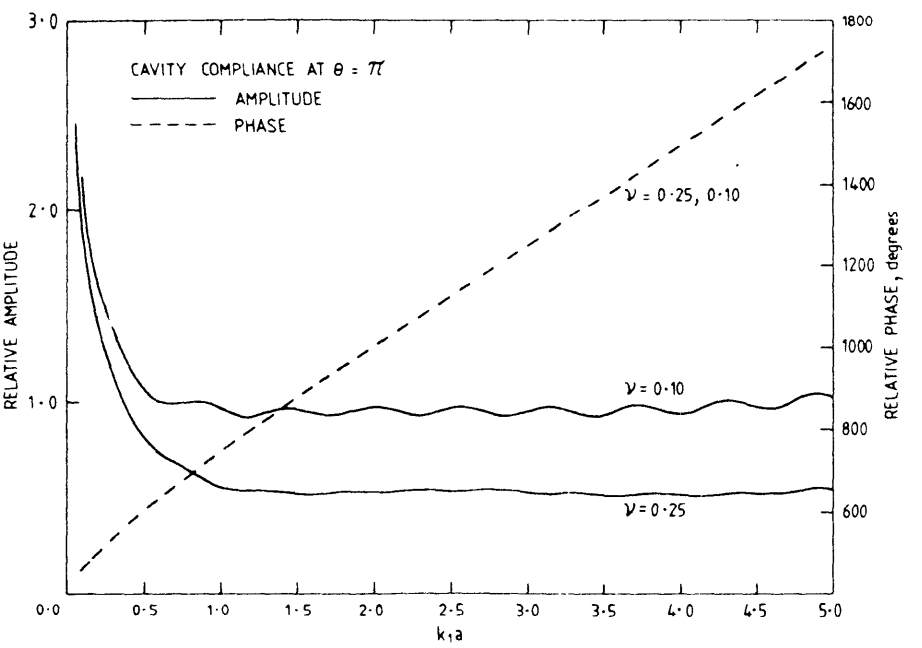

(d)

Figure 7 (continued) Compliance transfer functions (output displacement/input force) for the cavity wall at; (c) $\theta = 3\pi/4$, (d) $\theta = \pi$. The source is at the origin.

The impulse response of these transfer functions can be convolved with various stress pulses to calculate the associated radial-displacement waveforms of the cavity walls.

3.4 Point source on cavity wall

The three dimensional case of seismic radiation arising from a point source on the wall of a cylindrical cavity in an elastic medium has been examined by Greenfield (1978) and will be briefly discussed here. The analytical description is in the form of a Fourier - Bessel series and is an extension from the line-source treatment described above. Greenfield's notation (with some modifications) is used.

Figure 8 illustrates the coordinate system used. The components of particle displacement, u_r, u_θ and u_z, at a point in the medium, in terms of the cylindrical polar coordinates, r, θ, and z, are given by,

$$u_r = \frac{\partial \bar{\Phi}}{\partial r} + \frac{\partial^2 \bar{\Psi}}{\partial r \partial z} + \frac{1}{r}\frac{\partial \bar{X}}{\partial \theta}$$

$$u_\theta = \frac{1}{r}\frac{\partial \bar{\Phi}}{\partial \theta} + \frac{1}{r}\frac{\partial^2 \bar{\Psi}}{\partial z \partial \theta} - \frac{\partial \bar{X}}{\partial r} \qquad \text{---(35)}$$

$$u_z = \frac{\partial \bar{\Phi}}{\partial z} + \frac{\partial^2 \bar{\Psi}}{\partial z^2} + k_2^2 \bar{\Psi}$$

The potentials, $\bar{\Phi}$, $\bar{\Psi}$ and $\bar{X}$ obey the wave equations,

$$\nabla^2 \bar{\Phi} = -k_1^2 \bar{\Phi}$$

$$\nabla^2 \bar{\Psi} = -k_2^2 \bar{\Psi} \qquad \text{---(36)}$$

$$\nabla^2 \bar{X} = -k_2^2 \bar{X}$$

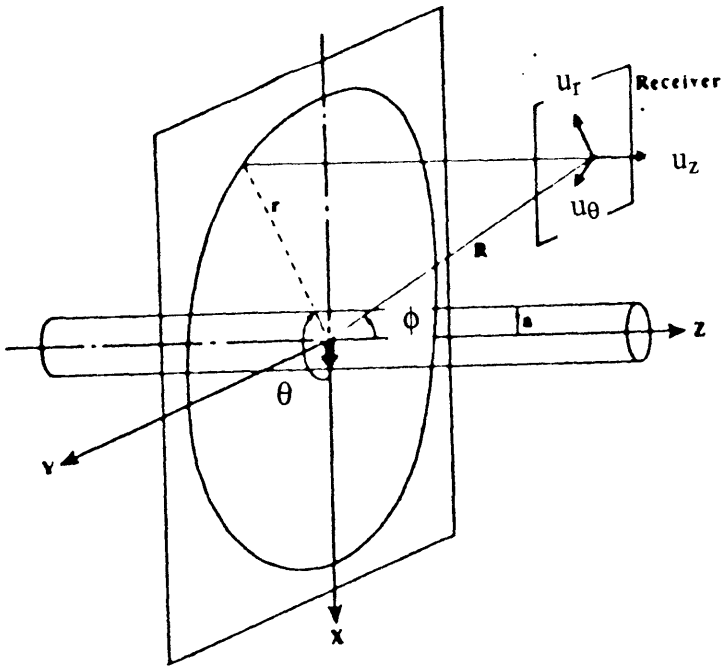

Figure 8. Geometry of the point source/cylindrical cavity interaction --after Greenfield (1978)

As in the 2-dimensional case, solutions for the potentials may be expressed in the form of the Fourier-Bessel series,

$$\bar{\Phi} = \sum_{l=0}^{\infty} \int_{-\infty}^{\infty} \Phi_l(k)\, dk$$

$$\bar{\Psi} = \sum_{l=0}^{\infty} \int_{-\infty}^{\infty} \Psi_l(k)\, dk \qquad \text{---(37)}$$

$$\bar{X} = \sum_{l=0}^{\infty} \int_{-\infty}^{\infty} X_l(k)\, dk$$

where,

$$\Phi_l = A_l(k)\, e^{ikz} H_l(\nu r) \cos l\theta,$$

$$\Psi_l = B_l(k)\, e^{ikz} H_l(\nu' r) \cos l\theta, \qquad \text{---(38)}$$

$$X_l = C_l(k)\, e^{ikz} H_l(\nu' r) \sin l\theta$$

The wave numbers, ν , and ν', are given by,

$$\nu = \sqrt{k_1^2 - k^2} \quad \text{and} \quad \nu' = \sqrt{k_2^2 - k^2}$$

(the wavenumber, ν, should not be confused with Poisson's ratio, ν).

The stresses at r = a are given by,

$$\sigma_{rr} = L\, \delta(z)\, \delta(\theta)\, \frac{1}{a}$$

$$= \sum_{l=0}^{\infty} L \int_{-\infty}^{\infty} D_l(k)\, e^{ikz} \cos l\theta\, dk, \qquad \text{---(39)}$$

$$\sigma_{r\theta} = \sigma_{rz} = 0.$$

where L is source "magnitude" and,

$$D_l(k) = L/(4\pi^2 a) \text{ for } l = 0,$$

$$D_l(k) = L/(2\pi^2 a) \text{ for } l \neq 0.$$

Thus, when the appropriate derivatives of the potentials are substituted into equations for the stresses (obtained from (35) using linear elasticity theory, as in the 2-dimensional

case) and the boundary conditions (39) are applied, equations for the coefficients, A_l, B_l, and C_l are obtained. In an analogous manner to the 2-dimensional case this can be expressed in matrix form as,

$$[G]\begin{bmatrix} A_l(k) \\ B_l(k) \\ C_l(k) \end{bmatrix} = \begin{bmatrix} D_l(k) \\ 0 \\ 0 \end{bmatrix} \qquad \text{---(40)}$$

The elements of **G** are g_{ij}. Expressing the dimensionless wavenumbers, νa, and ν'a by x and y gives;

$$\begin{aligned}
g_{11} &= \mu[-\frac{\lambda}{\mu} k_1^2 H_l(x) + 2H_l''(x)] \\
g_{12} &= \mu 2ikH_l'(y) \\
g_{13} &= \mu [\frac{2}{a} l H_l'(y) - \frac{2l}{a^2} H_l(y)] \\
g_{21} &= \mu 2ikH_l'(x) \\
g_{22} &= \mu(-2k^2 + k_2^2) H_l'(y) \qquad \text{---(41)} \\
g_{23} &= \mu \frac{l}{a} ikl H_l(y) \\
g_{31} &= \mu[-\frac{2l}{a} H_l'(x) + \frac{2l}{a^2} H_l(x)] \\
g_{32} &= \mu[-\frac{2}{a} ilkH_l'(y) + \frac{2ikl}{a^2} H_l(y)] \\
g_{33} &= \mu[\frac{-l^2}{a^2} H_l(y) + \frac{1}{a} H_l'(y) - H_l''(y)]
\end{aligned}$$

Thus, the complexity of the 3-dimensional case of the point source acting on the cavity wall is considerably greater than that of the analogous line-source problem. The added complexity arises from the necessity to incorporate an additional transform in the Fourier-Bessel formulation which allows for the z-dependence. This has the effect of making the

near-field evaluation difficult. In fact, Greenfield (1978) restricts his attention to the far-field with the use of the following far-field relation,

$$\int_{-\infty}^{\infty} I(k)\, H_l(vr)\, e^{ikz} dk \;\rightarrow_{R\rightarrow\infty}\; \frac{2e^{-ik_1R}}{R}\, i^{l+1}\, I\,(-k_1\cos\phi) \qquad \text{---(42)}$$

where I(k) is an arbitrary function of k. This simplification readily leads to the evaluation of the far-field displacement transfer function which can be shown to be equivalent to the far-field transfer function derived from the 2-dimensional case using seismic reciprocity principles. This will be discussed at greater depth in the following chapters.

The poles of the near-field transfer function relating cavity wall displacement to input stress will be indirectly related to the zeros of det.**G**. There is a further complexity involved in that additional Fourier transforms are required before the poles can be directly evaluated. Nevertheless, calculation of det.**G** yields lengthy expressions which include expressions of similar form to the Viktorov equation although the author is unaware of any attempt to extract the poles. The implication is that each Viktorov pole trajectory (in the 2-dimensional case, refer Fig. 5) will now form a surface of poles with the additional poles being associated with propagation down the borehole axis. However, the Rayleigh modes will still be dominant.

4. Dynamic Finite Element studies

4.1 Introduction

The Dynamic Finite Element Method (DFEM) is now a well established numerical solution procedure for many geophysical and engineering applications. The method, in the past had been largely restricted to modelling the vibrational response of foundations and structures, but was shown by Shipley et al. (1967) to be applicable to elastic wave propagation studies. Bathe and Wilson (1976) provide a comprehensive review of the Finite Element method including its application to dynamic problems The method is concerned with a spatial discretïsation of the problem under study to produce a grid or mesh. (A portion of a typical mesh is represented in Figure 9). This is followed by numerical time integration of the d'Alembert equation for equilibrium at each nodal point in the mesh to arrive at nodal displacements.

The relevant equations are in the form

$$\mathbf{L}\,\mathbf{u} = \mathbf{F}(t) \qquad \text{---(43)}$$

where **u** is a vector of nodal displacement and **F**(t) is a time dependent load vector. **L** is an operator of the following form,

$$\mathbf{M}\frac{\partial^2}{\partial t^2} + \mathbf{C}\frac{\partial}{\partial t} + \mathbf{K} \qquad \text{---(44)}$$

where **M**, **C** and **K** are mass, damping and stiffness coefficient matrices.

Belytscho and Mullen (1977) show that, with certain restrictions, solution of (43) is equivalent to solution of the elastic wave equations (1) and (2) in the form,

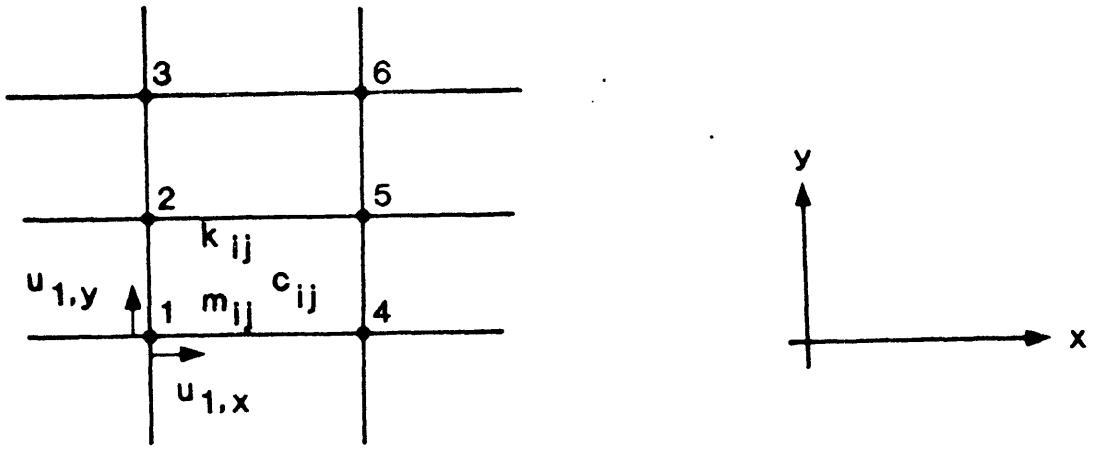

Figure 9. Portion of a typical DFEM mesh.

$$\nabla^2\Phi = \frac{1}{C_D}\frac{\partial^2\Phi}{\partial t^2}$$

$$\nabla^2\Psi = \frac{1}{C_S}\frac{\partial^2\Psi}{\partial t^2} \qquad \text{---(45)}$$

where, in the case of a Cartesian coordinate system, the Laplacian operator, ∇^2, is given by

$$\nabla^2 = \frac{\partial^2}{\partial x^2} + \frac{\partial^2}{\partial y^2} \qquad \text{---(46)}$$

Thus, DFEM can provide a convenient means of solving the elastic wave equations with little restriction on the complexity of the problem geometry.

4.2 Limitations of the method

In applications where elastic continua are spatially discretised, it is clear that particle motion with wavelengths shorter than the distance between nodal points cannot be accurately modelled. A regular mesh with 4 - nodes per element can be reasonably approximated by a single - pole, low-pass filter with the corner frequency given by 4-nodes per wavelength. Figure 10, from White et al (1977), shows the influence of element size per wavelength on mean - error in nodal displacement for one-dimensional wave propagation. Two element types were considered; a constant strain element (allowing linear displacement variation within the element) and a linear strain element (allowing quadratic displacement variation within the element).

Dynamic finite element models are susceptible to additional sources of error including dispersion, as indicated in Figure 11, internal reflections arising from aspect ratio contrasts between elements and from excessive gradation contrasts. Valliappan and Murti (1984) provide a recent review of these limitations.

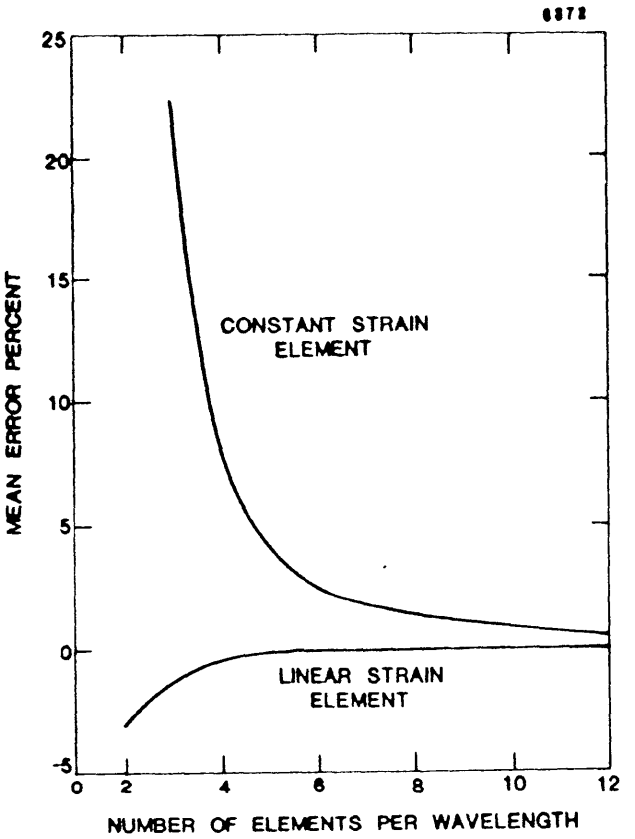

Figure 10. Influence of element size on mean error in nodal displacement for one dimensional wave propagation --after White et al. (1977)

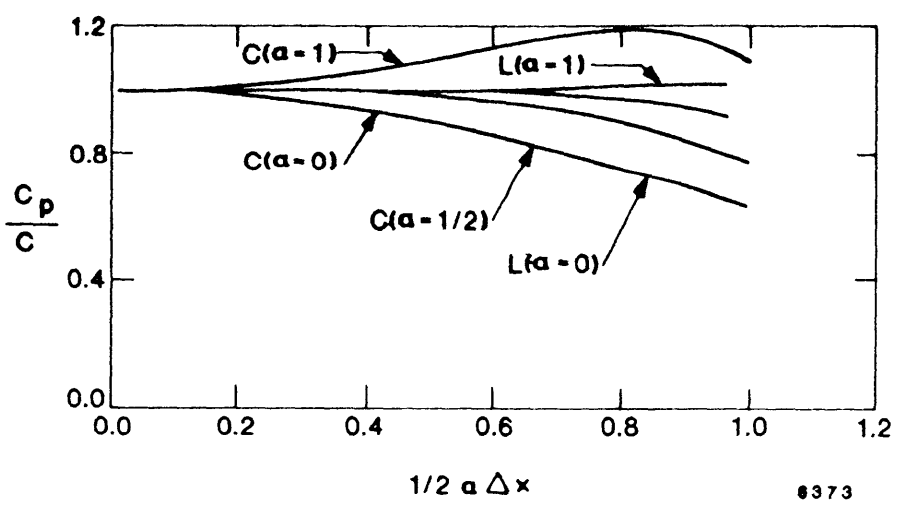

Figure 11. Dispersion as a function of wave-number,a, for constant strain, C, and linear strain, L, elements for lumped mass ($\alpha = 0$) and consistent mass ($\alpha = 1$) -- after Belytschko and Mullen (1977).

4.3 Representation of infinite media

The presence of artificial boundaries in finite element representations of wave propagation problems that require boundaries at infinity is unavoidable due to limitations of computer memory. These model boundaries can produce unwanted reflections of energy. However, model boundaries that absorb this incident energy, and thereby provide a representation of an infinite medium, can be approximated in DFEM with suitable nodal damping such as the "unified viscous boundary" described by Lysmer and Kuhlemeyer (1969) and extended by White et al. (1977). Figure 12 illustrates the effect on pulse reflection of changes to viscous boundary damping in a one-dimensional mesh.

Boundaries are said to be transparent to incident energy if stresses equal in magnitude, but opposite in sign to those caused by the arriving wave are applied at the mesh boundaries. This can be achieved by using the damping term in equation (43). Lysmer and Kuhlemeyer (1969) arrived at the following expression for boundary stresses,

$$\sigma_n = \alpha \rho C_D \dot{u}_n$$
$$\sigma_t = \beta \rho C_S \dot{u}_t \qquad \text{---(47)}$$

where α and β are dimensionless parameters and the subscripts, n and t, refer to normal and tangential components respectively. Lysmer and Kuhlemeyer (1969) found that $\alpha = \beta = 1$ will produce frequency independent absorbing boundaries with an efficiency of the order of 95%.

However, the above boundaries perform badly with angles of incidence less than 30°. White at al. (1977) extended the above approach by calculating α and β to give better incident angle independence. They give the following expressions for α and β,

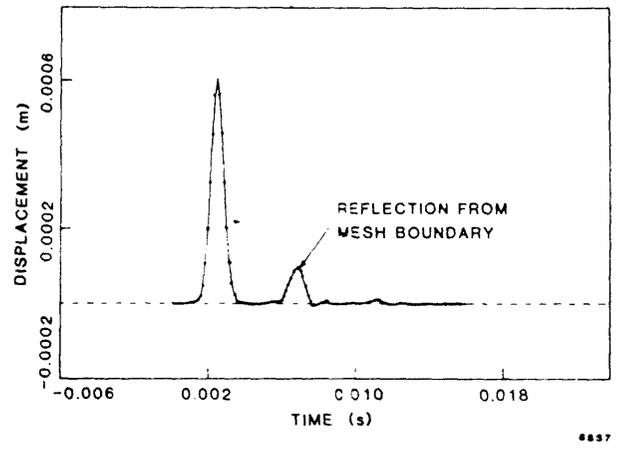

(a) damping is too "soft"

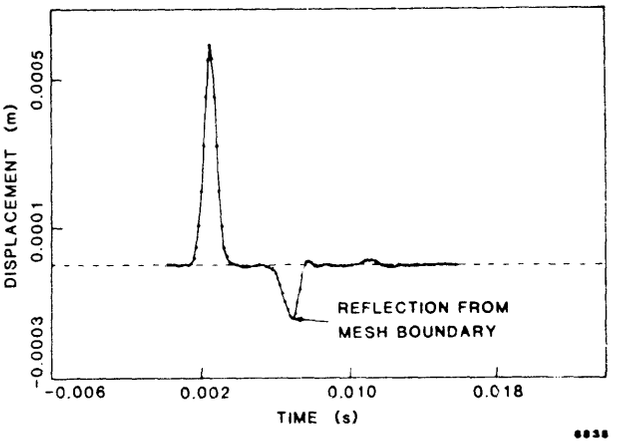

(b) damping is too "hard"

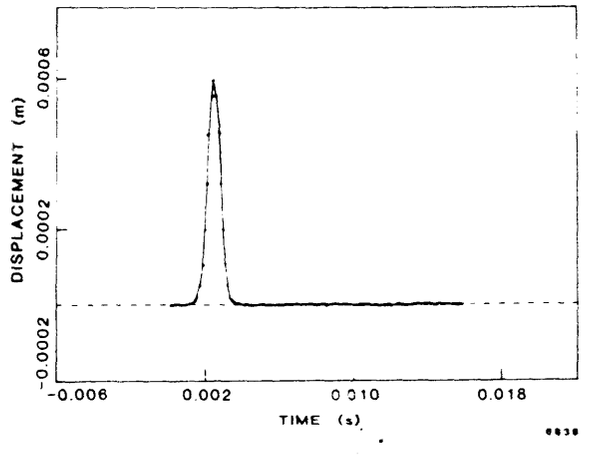

(c) damping is correct with little reflected amplitude, hence model adequately represents a portion of an "infinite" column

Figure 12. Response of a 1-dimensional DFEM model with viscous boundary damping to pulse input -- after Siggins (1983).

$$\alpha = \frac{8}{15\pi}\left[5 + 2s - 2s^2\right]$$
$$\beta = \frac{8}{15\pi}\left[3 + 2s\right] \qquad \text{---(48)}$$

where $s^2 = (1 - 2\nu)/2(1 - \nu)$ and ν is Poisson's ratio.

These boundary conditions can be implemented in DFEM computer programs such as ADINA (Bathe, 1975) with the use of concentrated nodal dampers. The values of the damping coefficients (for a particular node) are given by,

$$c_n = A\alpha\rho C_D \qquad \text{---(49)}$$
$$c_t = A\beta\rho C_S$$

where A is the effective area surrounding the nodal point in question.

4.4 Application of DFEM to a line-source on the surface of a half-space

The problem of a concentrated source acting on an elastic half space was first described by Lamb (1904) and is consequently known as Lamb's problem. (Mooney, 1974, has reviewed numerical solutions to a selection of Lamb type problems). As is stated elsewhere Lamb's problem represents a limiting case of the problem of a line-source acting on a cavity wall. It represents the case where wavelengths are small with respect to cavity radius.

The analysis described here begins with Lamb's (1904) solution for the normal component of the surface displacement resulting from a harmonic source, concentrated to a line, acting on the surface of an elastic medium. This solution is then extended in this dissertation (and by Siggins, 1982) by Fourier methods to that of a pulse line-source. The choice of a modified Gaussian function (with similar form to the Ricker pulse,

Robinson and Treitel, 1980) greatly simplifies the calculations. The resulting solution is then compared to the results of a DFEM analysis.

4.4.1 The Lamb solution

The normal surface displacement , u_n, is given by Lamb (1904) as,

$$u_n(x,t) = \frac{-iQ}{\mu} \frac{k_2^2(k_3^2 - k_1^2)^{1/2}}{F'(k_3)} e^{i(\omega t - k_3 x)} \qquad \text{(i)}$$

$$+ \frac{2iQ}{\mu} \left(\frac{2}{\pi}\right)^{1/2} \left(1 - \frac{k_1^2}{k_2^2}\right) \frac{e^{i(\omega t - k_2 x - \pi/4)}}{(k_2 x)^{3/2}} \qquad \text{(ii)} \qquad \text{---(50)}$$

$$+ \frac{iQ}{2\mu} \left(\frac{2}{\pi}\right)^{1/2} \frac{k_1^2 k_2^2}{(k_2^2 - 2k_1^2)^2} \frac{e^{i(\omega t - k_1 x - \pi/4)}}{(k_1 x)^{3/2}} \qquad \text{(iii)}$$

where Q is the line-source "magnitude".

F'(k) is the first derivative of the Rayleigh function, F(k), with respect to the generalised wave-number, k, where,

$$F(k) = (2k^2 - k_2^2)^2 - 4k^2(k^2 - k_1^2)^{1/2}(k^2 - k_2^2)^{1/2} \qquad \text{---(51)}$$

The roots of the Rayleigh equation,

$$F(k) = 0 \qquad \text{---(52)}$$

are the Rayleigh wave-numbers, k_3. Equation (51) is most conveniently expressed as a cubic in k^2 giving both real and complex roots. For the case of a Poisson solid the roots are real and $k_3 = k_2/0.9194$.

Thus the solution consists of three terms, (i), the Rayleigh wave term, (ii) the shear wave term and (iii), the longitudinal wave term. If the time dependence of (50) is ignored the resulting expression can be regarded as the transfer function of the half-space relating the surface normal displacement response to the line load. Denoting this transfer function by $U(\omega)$ it is then possible to calculate the half-space response to an arbitrary load-time function, p(t), by the following Fourier convolution integral

$$u_n(x,t) = \frac{1}{\sqrt{2\pi}} \int_{-\infty}^{\infty} P(\omega) \, . \, U(\omega) \, e^{-i\omega t} d\omega \qquad \text{---(53)}$$

where $P(\omega)$ is the Fourier transform of p(t). It should be noted that the three wave types in (50) are travelling in the negative x-direction. The choice of the sign convention shown in (53) results in waves travelling in the positive x-direction.

As shown in Siggins (1982) $u_n(x,t)$ is given by

$$u_n(x,t) = I_1 + I_2 + I_3 \qquad \text{---(54)}$$

provided $P(\omega)$ is an odd function of ω, where,

$$I_1 = -A \int_0^{\infty} P(\omega).\sin \omega(t + \frac{x}{C_R}) \, d\omega$$

- the Rayleigh pulse

$$I_2 = \frac{B}{x^{3/2}} \int_0^{\infty} \frac{P(\omega)}{\omega^{3/2}} \, . \, \sin \left[\omega(t + \frac{x}{C_S}) + \pi/4 \right] d\omega \qquad \text{--(55)}$$

- the shear pulse

$$I_3 = \frac{C}{x^{3/2}} \int_0^{\infty} \frac{P(\omega)}{\omega^{3/2}} \, . \, \sin \left[\omega(t + \frac{x}{C_D}) + \pi/4 \right] d\omega$$

- the compressional pulse

and the ω-independent constants, A, B and C are given by

$$A = \left(\frac{2}{\pi}\right)^{1/2} \frac{k_2^2 (k_3^2 - k_1^2)^{1/2}}{\mu F'(k_3)}$$

$$B = \frac{4}{\pi\mu}\left(1 - \frac{k_1^2}{k_2^2}\right)$$

$$C = \frac{1}{\pi\mu} \frac{k_1^2 k_2^2}{(k_2^2 - 2k_1^2)^2}$$

Depending on the form chosen for p(t) (and consequently, P(ω)) it is relatively straight forward to evaluate the integrals, I_1, I_2 and I_3 by numerical integration. The singularity in ω can be avoided by a suitable choice for P(ω); a suitable root of $1/x^{3/2}$ is chosen to give real displacements for the shear and compressional waves. The upper limit of integration can be estimated from the plot of P(ω) versus ω. Appendix 1 lists a FORTRAN program, LLDISP, which calculates $u_n(x,t)$ by numerical integration for each selected time step. The integration scheme is based on Patterson's rule (Patterson, 1967) and is a NAG5 (Oxford Univ., 1977) computer library routine, D01ACF.

4.5 A DFEM model of the line-source/half space problem

A rectangular finite element mesh with dimensions of 20 m x 35m was constructed from 4-node, constant strain, quadrilateral elements. A high degree of element refinement was introduced near the central portion of the upper mesh boundary, i.e.,at the location where the forcing pulse was to be applied. Material properties representative of sedimentary rock were allocated to the elements. These properties were,

Lame's constants, $\lambda = \mu = 8 \times 10^9$ Pa.,

Density, ρ 2.5×10^5 kg/m^3

(Poisson's ratio, ν, = 0.25)

The phase velocities of compression, C_D ,and shear waves, C_S, given by equations (2)

are respectively 3098 m/s and 1789 m/s.

The average element size in the mesh was 2m. This implies that the spectral content of the forcing pulse applied to the mesh should not contain significant amplitude at frequencies in excess of 2000 radians/sec.

DFEM analyses were then carried out using the general purpose finite-element program ADINA (Bathe, 1975). The consistent mass formulation was used since, in general, higher accuracy can be achieved for wave propagation studies. Newmark's method was used for time integration (Newmark, 1959). Prior to the line-source study the response of the mesh, including viscous boundary damping applied to the lower mesh boundary, was checked by driving the upper boundary with a uniform pressure pulse. The pressure-pulse waveform applied was in the form of a derivative of a Gaussian ,

$$p(t) = -2b^2 t\, e^{-b^2 t^2} \qquad \text{---(56)}$$

where b is a constant determining pulse band-width; t (time in seconds) can be replaced by $t - t_0$, where t_0 is an arbitrary time shift.

The displacement waveform of the resulting plane compressional wavefront can be determined from basic geophysics as

$$u(t) = -\frac{1}{\rho C_D} \int_{-\infty}^{t} p(t)\, dt \qquad \text{---(57)}$$

Application of (57) to (56) yields

$$u(t) = \frac{1}{\rho C_D}\, e^{-b^2 t^2} \qquad \text{---(58)}$$

Figure 13(a) presents the displacement response of the upper mesh boundary, both theoretical (according to equation (58)) and predicted by the DFEM model. In this case there is no boundary damping present and an in-phase reflected pulse returning from the bottom boundary of twice the incident amplitude should be present as is indeed the case. Figure 13(b) presents the response of the mesh with boundary damping present with dashpot constants of various values including those calculated from the equations of White et al. (1977). Thus the DFEM model, with appropriate boundary conditions, provides an accurate representation of a semi-infinite medium.

4.5.1 The choice of driving pulse for the line-source

Since, as discussed earlier, DFEM models will behave dynamically as low-pass filters, any applied forcing pulse has to be band-limited in accordance with those frequency constraints. A convenient forcing pulse for the line-source is a modified Gaussian,

$$P(\omega) = \omega^3 e^{-B\omega^2} \qquad ---(59)$$

where B is a constant determining band-width. The time-domain form of (59) is of the form,

$$p(t) = t(1 - Ct^2) e^{-Dt^2} \qquad ---(60)$$

where, as with the previous pulse, t can be replaced with $t - t_0$. Figure 14 presents this pulse and its Fourier transform. The above pulse has disadvantages from filter theory considerations in that it is not strictly causal ; i. e., it is not physically realisable as a time waveform since a time-shifted form of (60) will have non-zero amplitude at times less than zero due to the asymptotic manner of the approach of the tails of the pulse to zero. This disadvantage can be overcome by forcing (60) to zero at times ≤ 0. This produces a small departure in the phase spectrum from linear phase. Theoretical waveforms arising from this pulse were generated using LLDISP to evaluate equations (55). Comparisons between theory and DFEM results will be presented in Chapter 5.

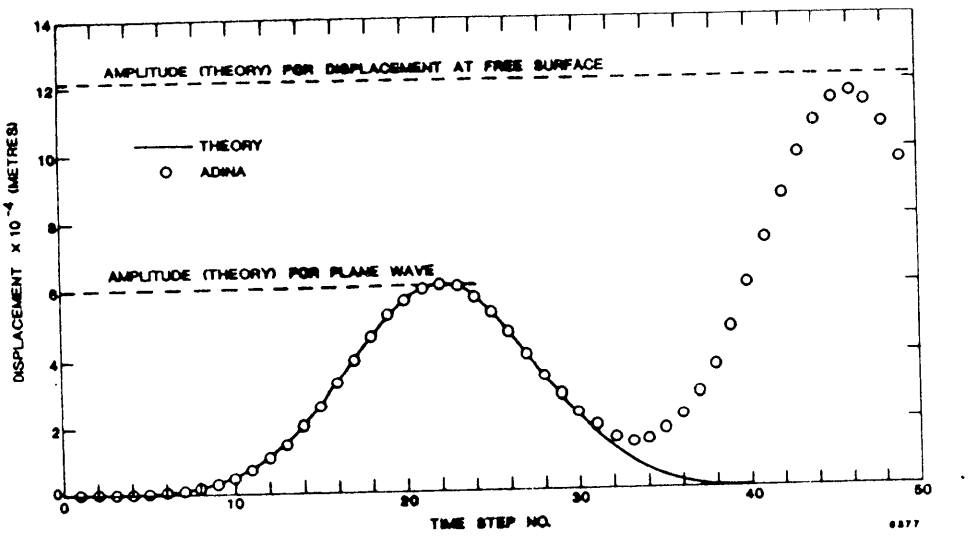

(a)

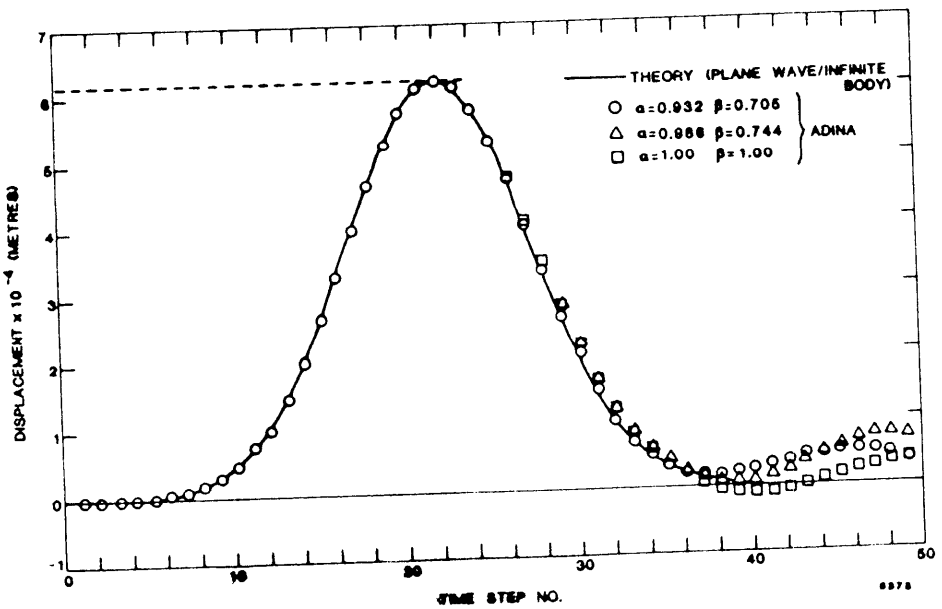

(b)

Figure 13. Displacement response of a DFEM model representing a half-space with trial values of viscous boundary damping; (a) no damping (b) with various damping.

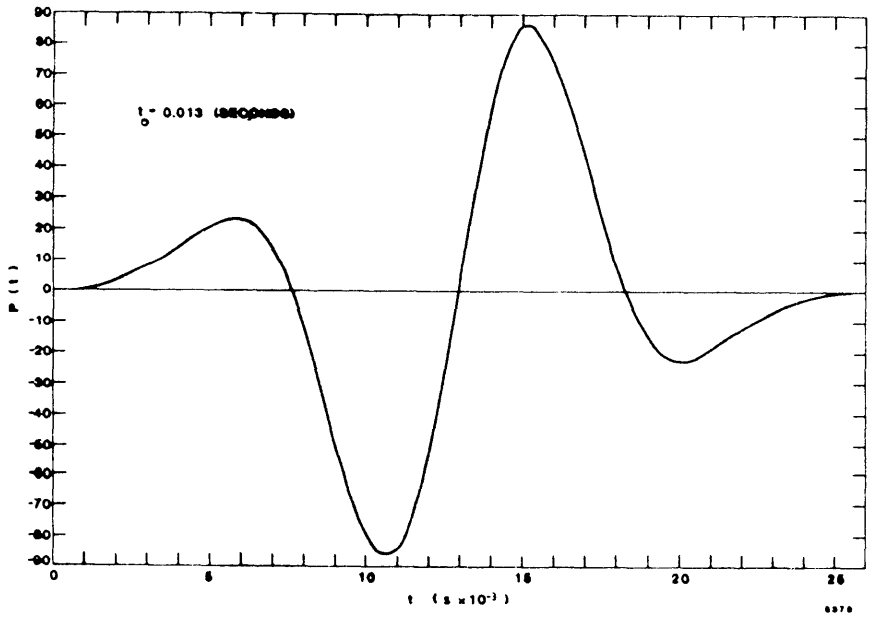

(a)

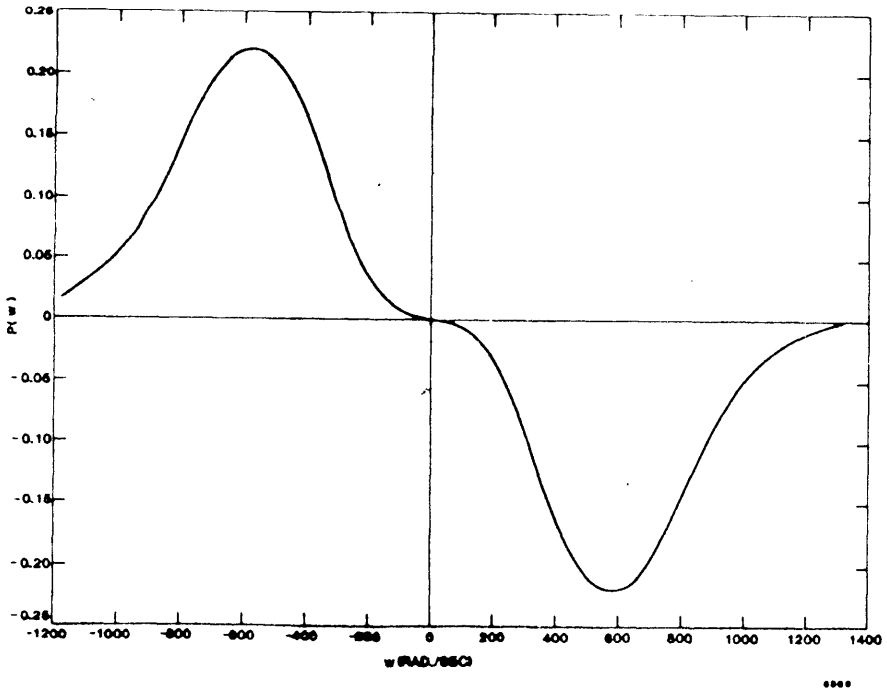

(b)

Figure 14 (a) A "Gaussian" source pulse. (b) Its Fourier transform.

4.6 A DFEM model of a line-source on the wall of a cavity in an infinite medium

The geometry (refer to Figure 4) in the line-source/cavity interaction is symmetric about a plane bisecting the cavity and co-incident with the source, so it is only necessary to consider a semi-circular mesh. In the near-field displacement gradients are high, so a high level of spatial discretisation is required near the source in contrast to the outer regions of the mesh. To avoid aspect ratio contrasts, the aspect ratio for all elements was fixed at 1.5:1. This results in the following equation describing nodal point locations along a radius at $\theta = 0$:

$$r_i = a(1 + 1.5\varepsilon/a)^{i-1} \qquad \text{---(61)}$$

where,

$i = 1, 2, 3,..., j$

j is the number of rings of elements required,

a is cavity radius,

ε is the element size.

For example, if 48 elements are required around the semicircle,

$$\varepsilon = \pi a/48$$

Selecting $j = 26$ and rotating the nodal intercepts through π radians in increments of $\pi/48$ gives a semicircular mesh with 1274 nodes and 1200, 4-node elements. Elements increase in size geometrically according to equation (61) as the outer boundary is approached. The outer boundary is at approximately 10.4 a. Figure 15 presents a portion of the resulting mesh.

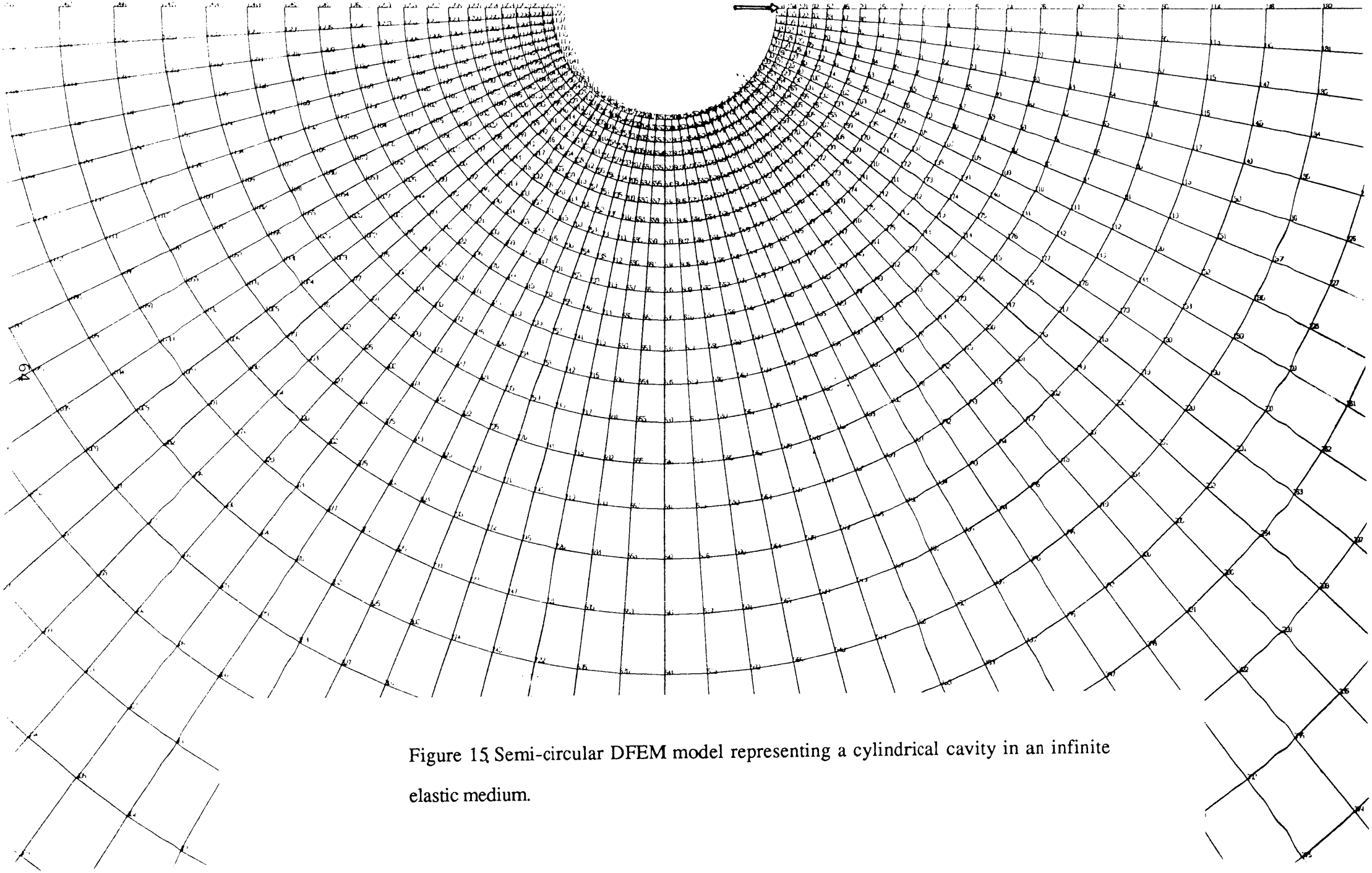

Figure 15 Semi-circular DFEM model representing a cylindrical cavity in an infinite elastic medium.

4.6.1 Boundary conditions.

Viscous dampers, acting both radially and tangentially, were used on the outer mesh nodes with dashpot constants calculated from the equations of White et al. (1977), equations (48). No nodal points were fixed; however, nodes lying on the axis of symmetry were constrained to displace in the r-direction only. The mesh is thus unconstrained in the r-direction which imposes restrictions on the types of driving pulse allowed. In particular, any d.c. component (0 Hz) will result in acceleration of the mesh as a whole. The pulse described in (60) satisfies the requirement of zero d.c component and was used to drive the cavity wall. Figure 16(a) illustrates the pulse waveform plotted against dimensionless time ; in 16(b) the force pulse spectrum is superimposed on the DFEM cavity-model filter characteristics.

As in the previous case DFEM solutions were performed using the general purpose finite element program, ADINA (Bathe, 1975). A variety of meshes with differing numbers of elements (ranging from 24 to 48) around the semi-circle were used. All analyses were run on a Cyber 76 computer with solution times (cpu times) of the order of 100 seconds. However, the analysis described here was carried out with 48 elements around the semi-circle, i.e., a total of 1200, 4-node, constant strain, elements for the mesh as a whole. Material properties assigned to the elements were representative of rock encountered at an experimental site (the Broken Hill site, described more fully in chapter 8). Laboratory tests on rock cores taken from this site were used to establish the elastic constants. Since there was some discrepancy between static and dynamic Poisson's ratio, ν was taken to be 0.1. These elastic constants result in C_D and C_S equal to 4730 m/s and 3154 m/s respectively. The consistent mass formulation was used and Newmark's method was used for the time integration (Newmark, 1959). Comparisons between analytical and DFEM predictions are presented in the following chapter.

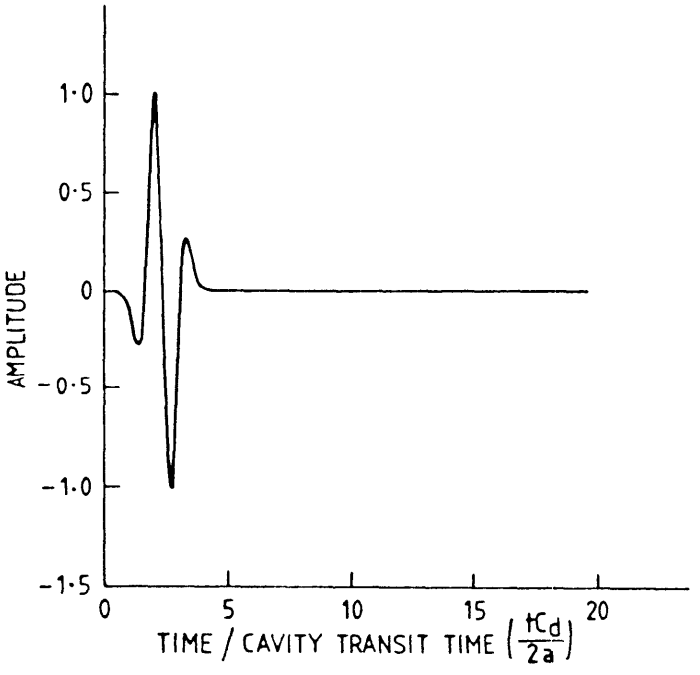

(a)

Figure 16 (a). Waveform of line-source pulse applied to cavity wall.

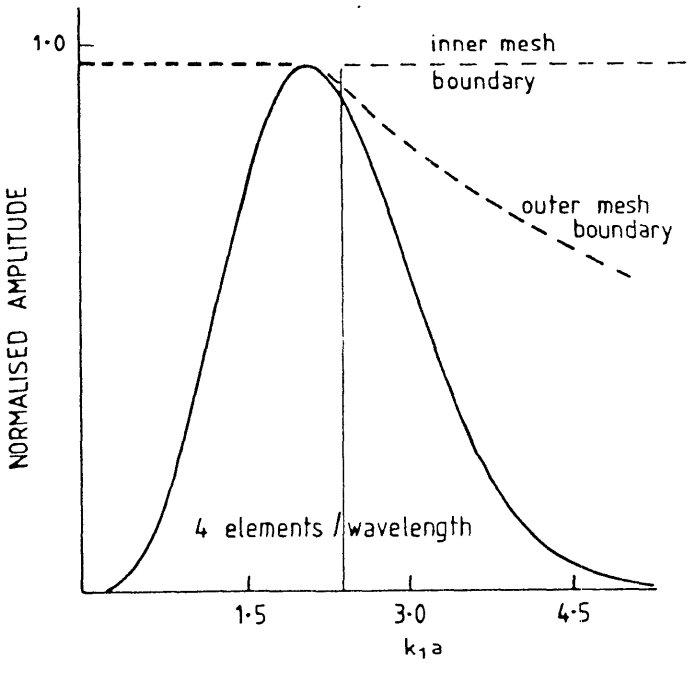

(b)

Figure 16 (b) Source pulse spectrum superimposed on DFEM mesh filter characteristics.

5. Comparisons between theory and DFEM solutions

5.1 Line source on a semi-infinite medium

When the analytical solution for the line-source on a semi-infinite medium (equations 54 and 55) is examined it can be seen that as x approaches zero the shear and compressional displacements approach infinity. This is in agreement with the static case for a line-load on the surface of a half-space with x approaching zero where,

$$u_n \alpha \log(x)$$

(Timoshenko and Goodier, 1970). Displacements also approach infinity for all values of x as ω approaches zero. However, this singularity can be avoided by restricting the driving pulse to odd functions of ω . This is the basis of the derivation presented in Siggins (1982).

With the finite element model singularities will be avoided because of limitations associated with finite-element size. In particular, with the constant strain elements used, displacement variation within the elements will be linear and thus the solution accuracy will decrease markedly near the source. Figure 17 presents a plot of theoretical peak surface displacements (calculated with LLDISP) and the corresponding DFEM results versus distance from the source. Two pulse bandwidths, B1 and B2, were investigated. It is clear that the DFEM solution approaches the Rayleigh asymptote rapidly, i.e., at much smaller values of x than the theoretical predictions. This is undoubtably due to the smoothing effects of the small elements near the source which remove the singularity by effectively increasing the loaded area. This reduces the stresses and consequently the displacements to finite values at the source. Nevertheless, the far-field solution (the Rayleigh component which is not attenuated with distance from the source in the two-dimensional case) is accurately predicted for both pulse band-widths.

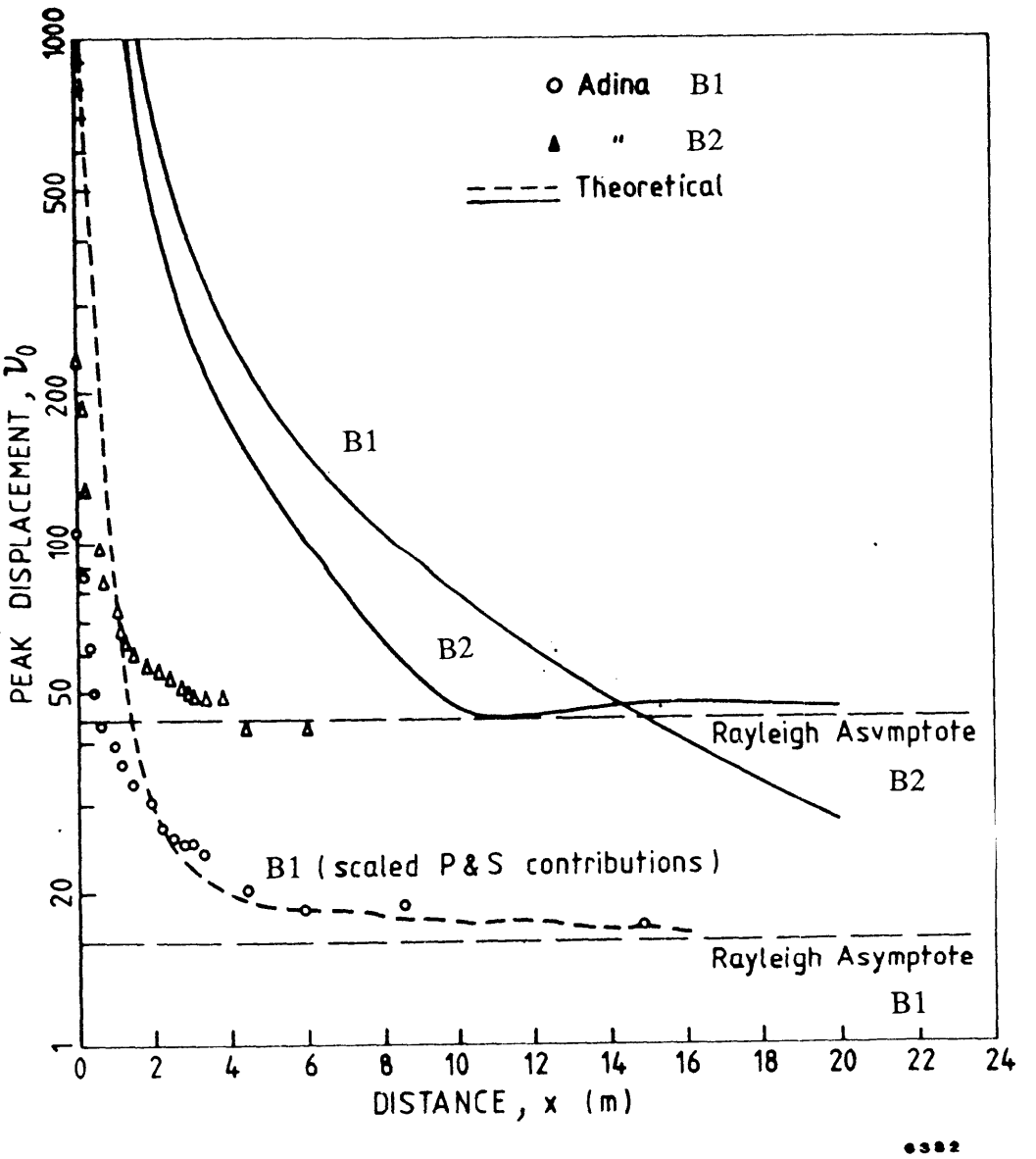

Figure 17. Peak surface displacement (arbitrary units) versus distance from a line source. A comparison between theory and DFEM results. Oscillations in the tail of theoretical curves are due to the superposition of wave modes with differing phase.

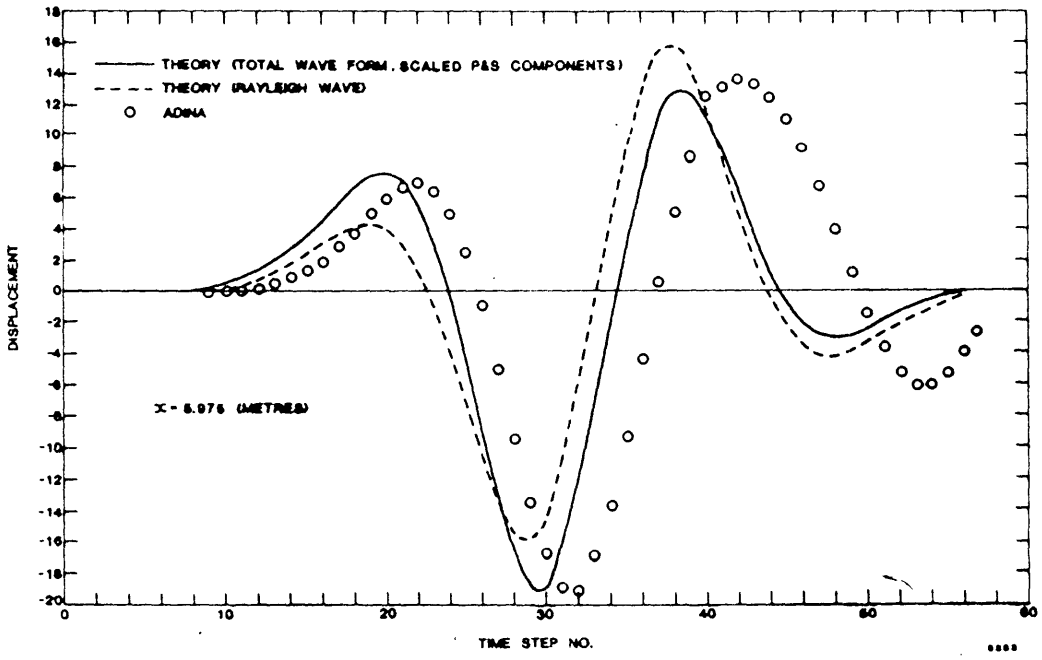

Figure 18. Comparisons between theoretical displacement waveforms and DFEM predictions.

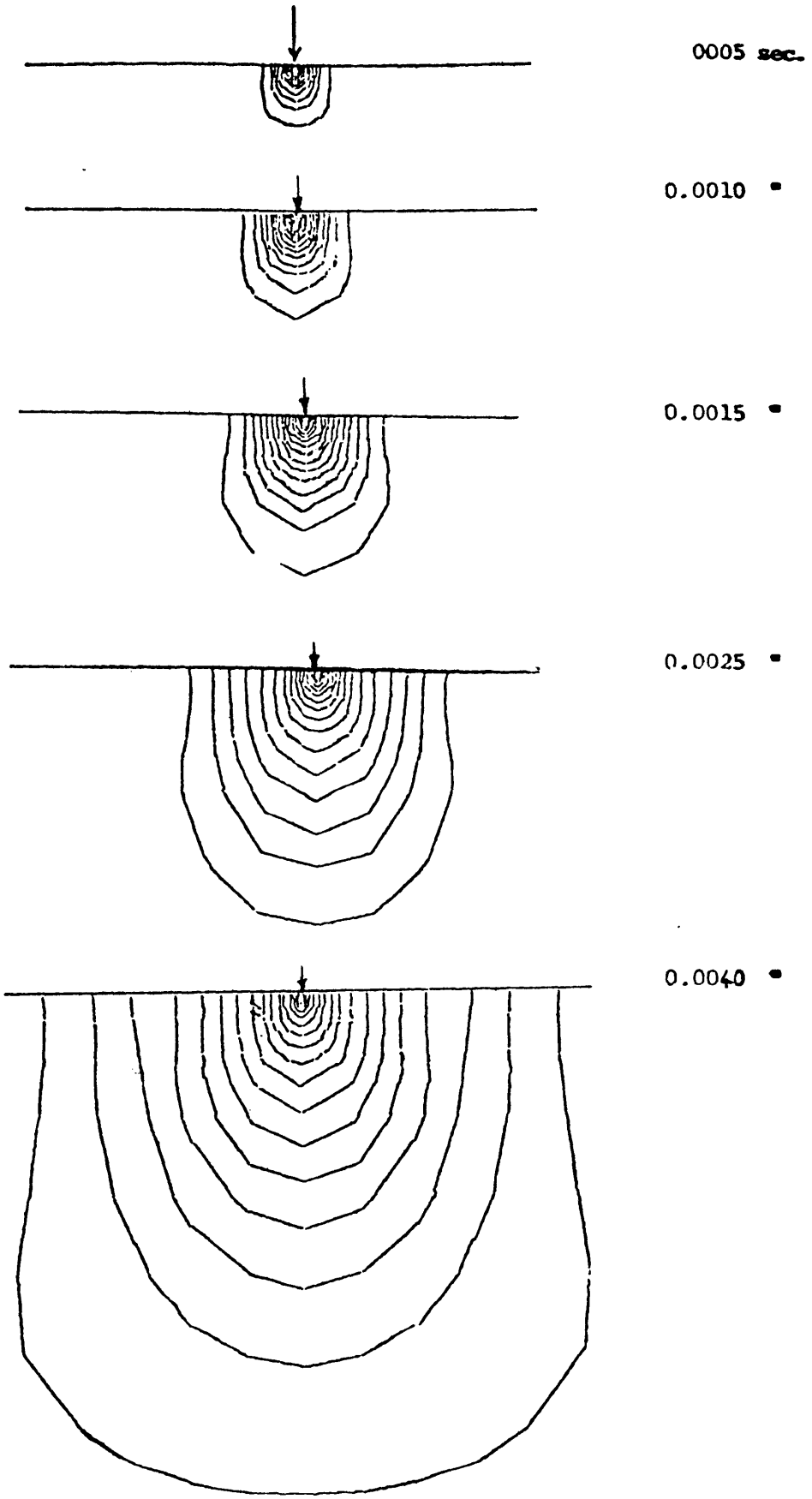

Figure 19. DFEM model of propagation of a cylindrical wavefront into an elastic half-space. Contours of equal displacement (using FEVECO, Perkins, 1980) are shown at various solution times.

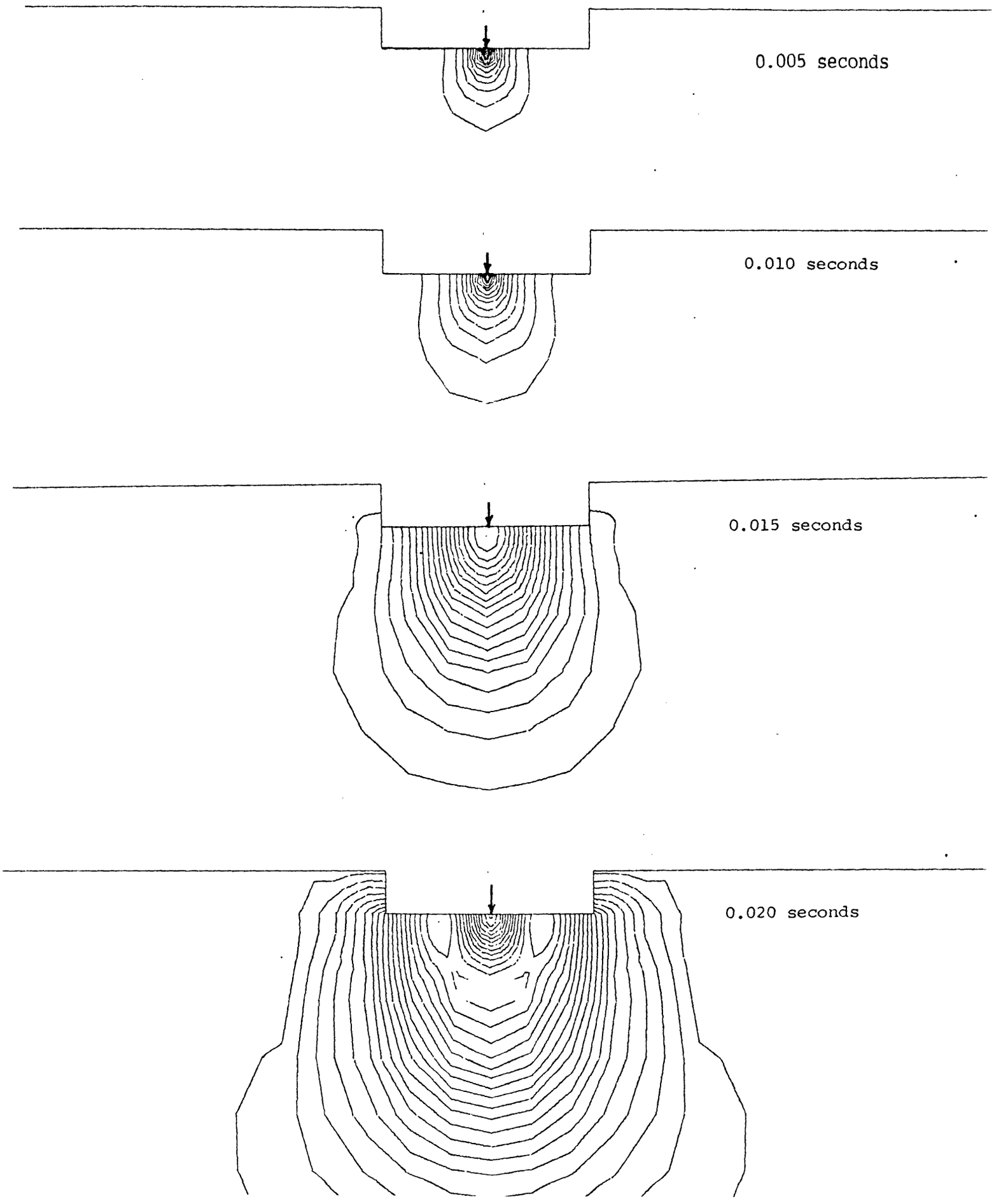

Figure 20. DFEM model of propagation of a cylindrical wavefront into an elastic half-space with a rectangular cut-out. Contours of equal displacement are shown at various solution times.

Better agreement between theory and DFEM predictions in the near-field can be obtained by reducing the theoretical compressional and shear wave amplitudes using empirical scaling constants as is also indicated in Figure 17. (This approach is put on a more rigorous basis in the discussion of the near-field behaviour of the line-source on the cavity wall.)

Figure 18 present displacement waveforms, both theoretical (with scaled P and S components) and DFEM. The propagation of the disturbance into medium, as predicted by the DFEM models, is presented in Figure 19.

A major strength of DFEM is the ability to model complicated geometries with relative ease. Figure 20 presents the propagation of a disturbance into an infinite elastic medium with a rectangular cut-out. This model can also represent the excitation of an opening in an elastic medium, such as a mine-tunnel of rectangular cross section, by a pulse applied to the floor or roof. The presence of standing waves on the opening is clearly indicated on the displacement contour plots at long solution times.

Thus the DFEM model of the line-source/half-space problem, whilst not performing accurately near the source, produced accurate far-field solutions and served to point out restrictions of the method when attempting to model problems which have singular behaviour. The analysis was valuable in that it suggested methods of dealing with the near-field behaviour which would be of use in the DFEM analysis of the line-source/ cavity interaction

5.2 Line source on cavity wall

5.2.1 A comparison of the DFEM results with a theoretical solution for the far-field

A seismic reciprocity approach, similar to that described by White (1960) and Greenfield (1978), can be invoked to describe the far-field plane wave arising from a line-source acting on the cavity wall. Figure 21 illustrates the seismic reciprocity between stress and displacement at two points in an elastic medium containing a cavity.

A Fourier-Bessel series solution for the interaction of plane compressional wave with a cylindrical cavity has been described by Pao and Mow (1973). This series solution was evaluated numerically by Blair (1984) for large wavenumbers. It can be regarded as a transfer function relating displacement of the cavity wall to the incoming compressional wave displacement. This solution, in the form of a computer program, was kindly made available to the author. The computer code was adapted to run on a Hewlett-Packard 1000 F-series processor. The displacement-ratio transfer-function for the wave-incident side of the cavity is presented in Figure 22 for a cavity in an elastic medium with Poisson's ratio equal to 0.1. The transfer-function was then evaluated as a "compliance" transfer-function relating output displacement to input stress for the wave-incident side of the cavity.

With the use of the transfer-function in this form it is now possible to calculate the far-field displacement waveform travelling away from the cavity arising from the application of a line-pressure pulse to the cavity wall. As can be seen from Figure 21 this is achieved by a Fourier convolution of the driving pulse (Figure 16 ; equation 60) with the impulse response of the compliance transfer-function. The result of this convolution,

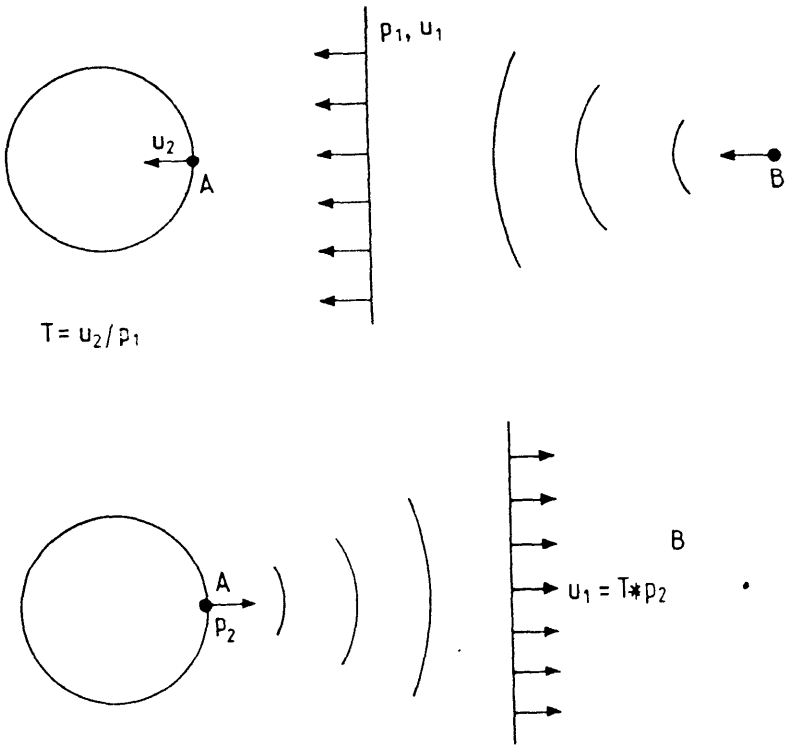

Figure 21. Seismic reciprocity between stress and displacement at two points (A and B) in an elastic medium can be used to obtain the far-field displacement waveform at B due to a source at A if the transfer function T is known.

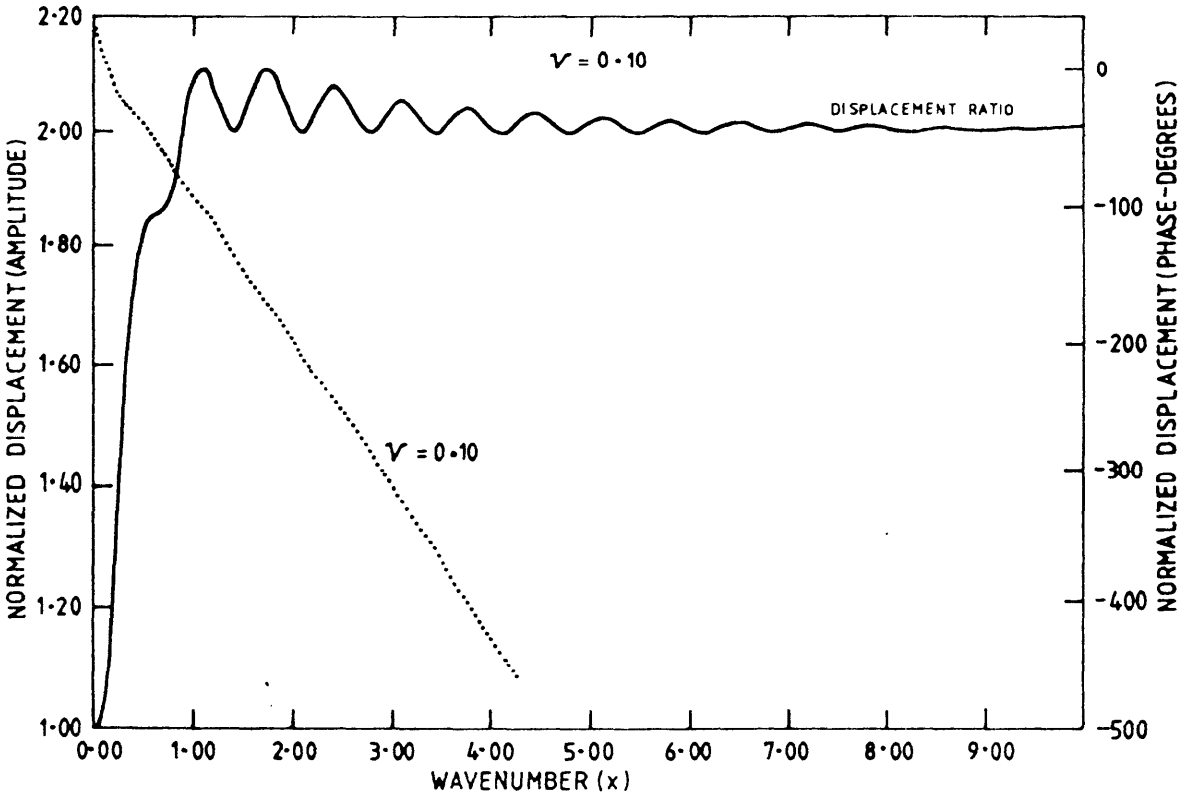

Figure 22. Transfer function relating cavity wall (wave incident side of the cavity) displacement response to incoming compressional wave displacement.

carried out with the use of the Fast Fourier transforms described by Singleton (1967), is presented in Figure 23(a) and (b).

Figure 23(c) presents the theoretical waveform obtained in this manner together with the normalised DFEM predicted waveform near the mesh outer boundary (r = 9.8a). Agreement is acceptable with discrepancies most probably due to the fact that r = 9.8a is not sufficiently far from the cavity to be "far-field".

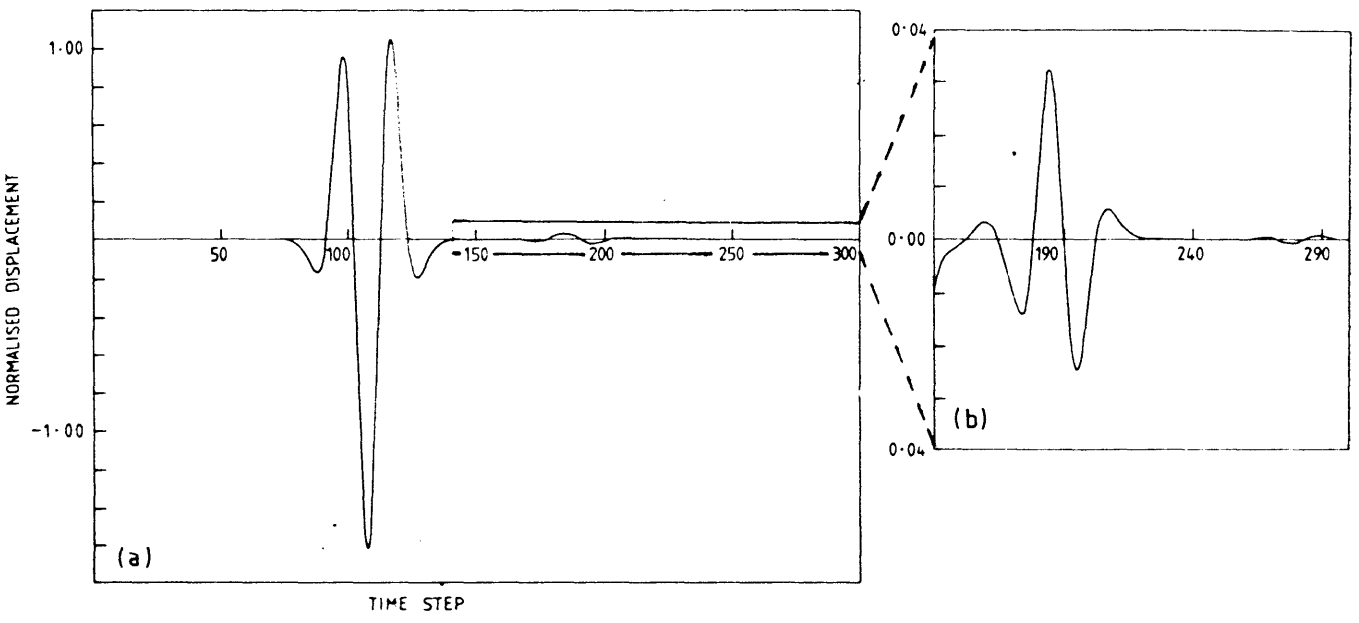

Figure 23 (a). The far -field displacement waveform obtained using seismic reciprocity . The tail of the waveform is shown magnified in (b). Approximately twenty time -steps correspond to the cavity transit time $2a/C_D$.

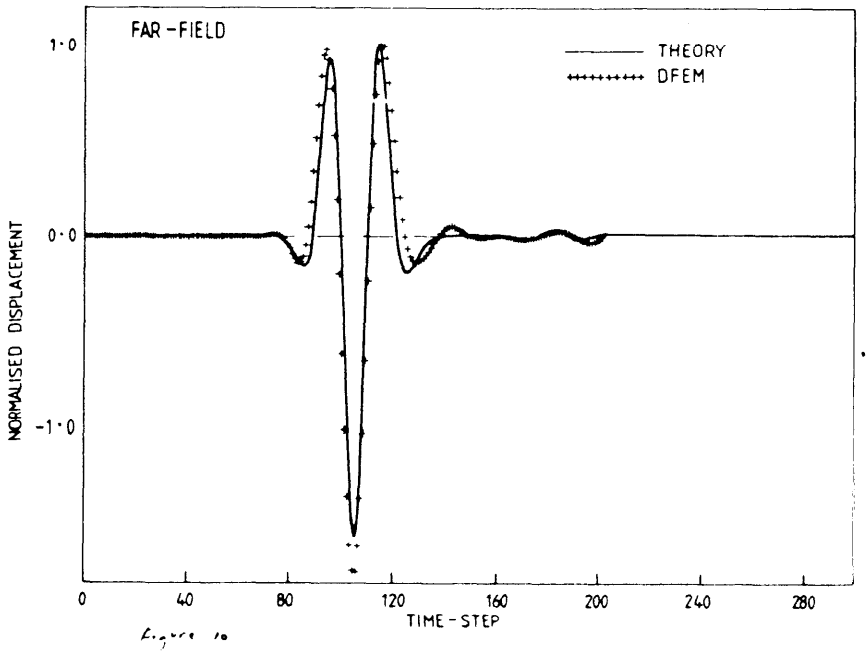

Figure 23 (c). DFEM predicted waveform at r = 9.8a and the analytical waveform.

5.2.2 Near-field (r = a) analytical and DFEM predictions

Normalised radial displacement waveforms at θ values of π/4, π/2, 3π/4 and π, both analytical and predicted by DFEM, are presented in Figures 24(a) to 24(d). The analytical waveforms were calculated by Fourier convolutions of the driving pulse (equation 60) with the impulse response of the respective complex compliance transfer functions (presented in Figures 7 (a) to 7(d)).

In the analytical case as θ approaches zero, u_r will tend to infinity. This is manifested in the failure of the series solution (32) to converge as θ nears zero. As discussed in the case of the DFEM model of the line-source/half space interaction, this singularity is smoothed in the DFEM analysis due to finite element limitations. The analytical solution for the line-source cavity interaction can be adapted to describe the compliance at θ = 0 in manner that allows comparisons with the DFEM results at θ = 0.

Consider a load distribution, A(ω,θ), concentrated about θ = 0. Let the transfer function for u given by the series (32) be represented by T(ω,θ). Then the amplitude response at θ is given by

$$u_r(\omega,\theta) = (A*T)\, e^{-i\omega t} \qquad ---(62)$$

where the asterix denotes convolution. If T is represented by a smoothly varying component, T_1 and a singular component, T_2 and if A(ω,θ) can be separated as $A_1(\omega)\, A_2(\theta)$, it is possible to show for θ = 0,

$$u_r(\omega,0) = \left[T_1(\omega,0)\bar{A}(\omega) + K\bar{A}(\omega) \right] e^{-i\omega t} \qquad ---(63)$$

where $\bar{A}(\omega)$ represents total load and K is a constant independent of ω . This is the

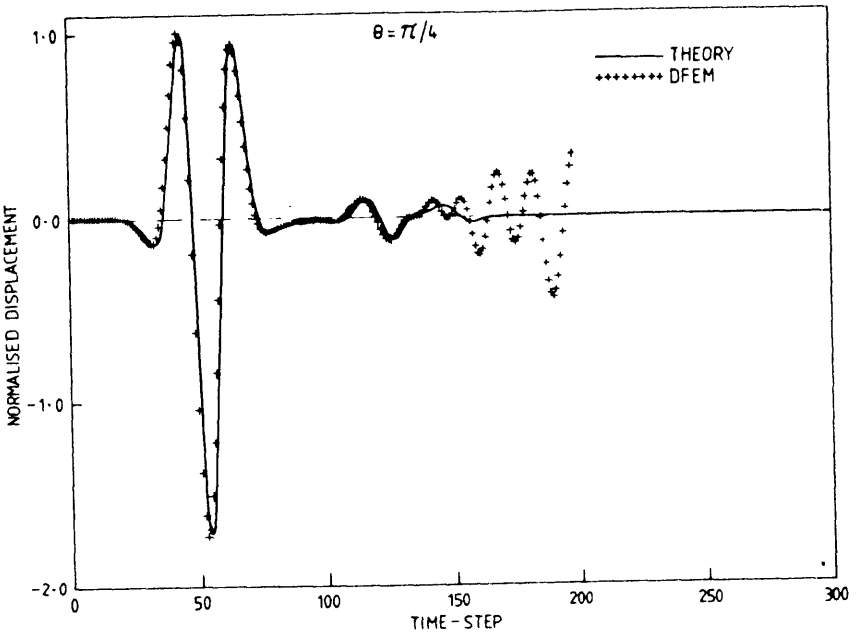

(a)

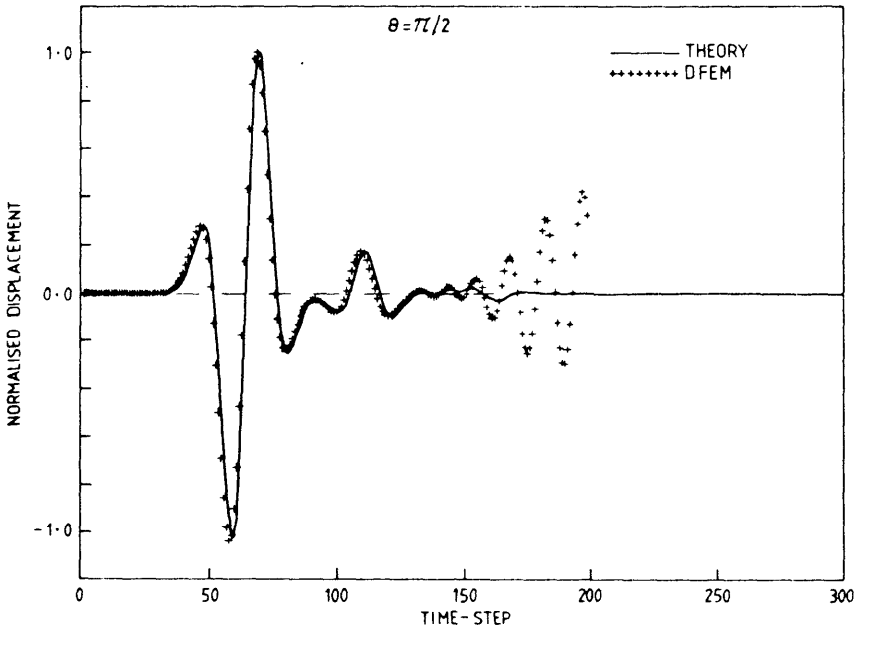

(b)

Figure 24. Radial displacement waveforms , both analytical and predicted by DFEM, arising from a "Gaussian" source pulse at the origin. The displacement waveforms are at; (a) $\theta = \pi/4$, and (b) $\theta = \pi/2$.

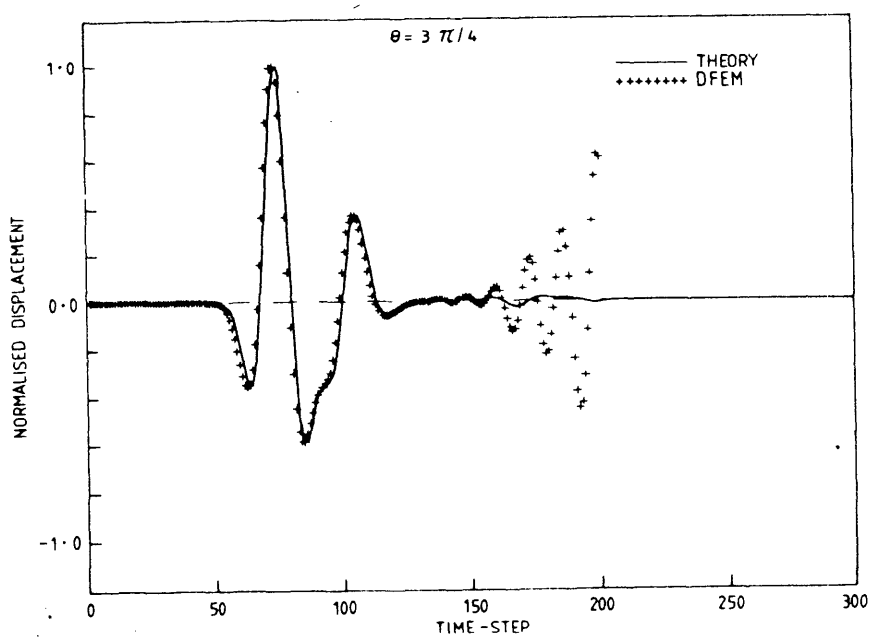

(c)

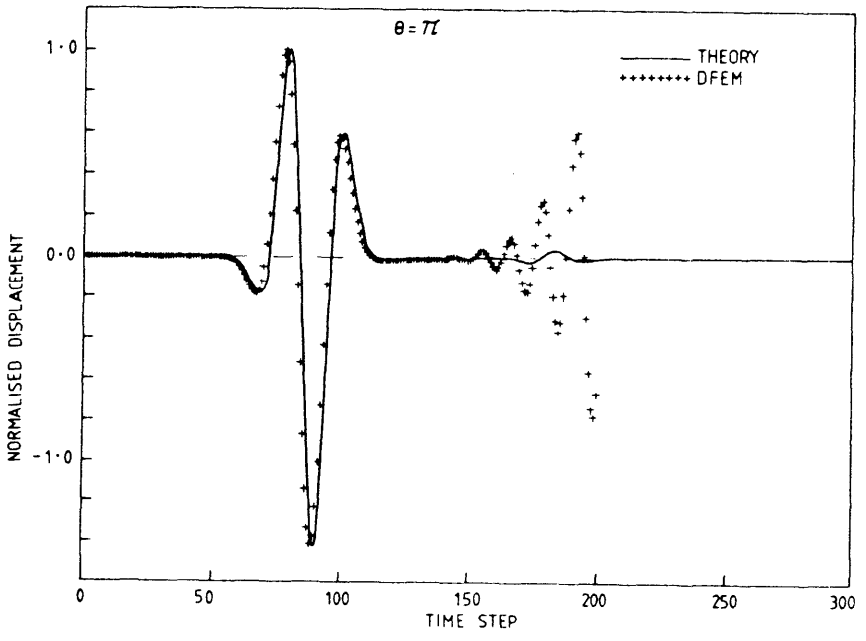

(d)

Figure 24 (continued) Radial displacement waveforms , both analytical and predicted by DFEM, arising from a "Gaussian" source pulse at the origin. The displacement waveforms are at; (c) $\theta = 3\pi/4$, and (d) $\theta = \pi$.

justification for deriving a convergent series at $\theta = 0$ from (32) by subtracting the ω - independent expression described in Chapter 3.3.

In general, however, equation (32) will be multiplied by a complex constant so that phase can be incorporated. Thus, both amplitude and phase components of K are required for comparison with the DFEM results at $\theta = 0$. A convenient method of evaluating K is to convolve the impulse response of the convergent series for T at $\theta = 0$ with a pulse possessing a well-defined onset such as the impulse response of a Butterworth filter[1], B(f), defined by,

$$|B(\omega)|^2 = 1/\left[1 + (\omega/\omega_c)^{2n}\right] \qquad ---(64)$$

where n is the order of the filter and ω_c is the selected cutoff (-3db) point of the filter.
A poor guess for the amplitude of K will appear after convolution as a superposition of an additional pulse, thereby distorting the onset of the displacement pulse. The amplitude of K can therefore be adjusted until a displacement waveform with a similar well defined onset results from subsequent convolutions. The phase component of K can be determined from the phase lag between the input pulse and the DFEM results.

This process was followed and yielded the compliance transfer function for $\theta = 0$ presented in Figure 25. This dynamic compliance is then applicable to a cavity excited at the origin by a source distributed over a small extent in θ sufficient only to remove the singularity in the stresses and displacements. (Smoothing of singularites will also occur experimentally due to the finite width of any loading device). Consequently, direct comparisons can be made with this transfer function and the DFEM model.

Theoretical displacement waveforms, obtained by convolving two load pulses in turn with the impulse response of the above transfer function, together with the corresponding finite element waveforms at $\theta = 0$ are presented in Figure 26. The two

source pulses were, (a) the modified Gaussian and (b) the impulse response of a fourth order (n = 4) Butterworth filter with the cut-off frequency selected at $k_1a = 1.33$.

1

The impulse response of the Butterworth filter described above, although a causal pulse, is not suitable as a driving pulse for the DFEM model for solution times exceeding $10.4a/C_D$ since the pulse has significant energy at 0 Hz which will eventually produce acceleration of the mesh as a whole.

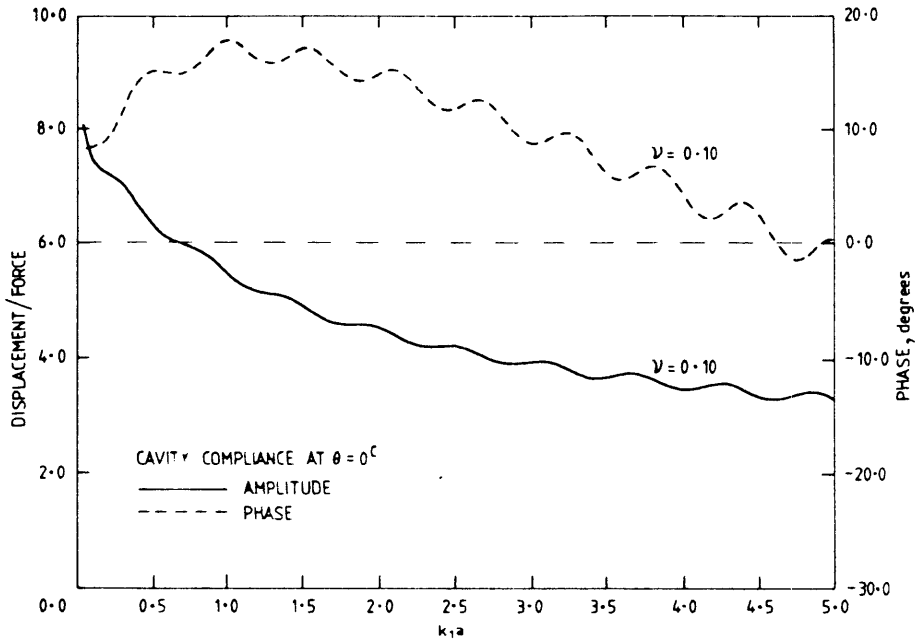

Figure 25. Cavity compliance at $\theta = 0$ due a force distributed over a small extent in θ.

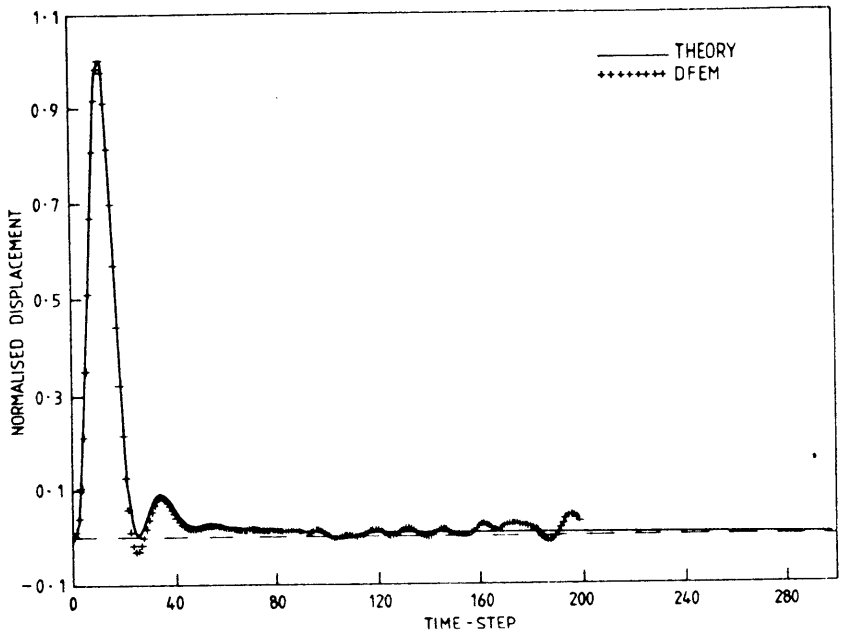

(a)

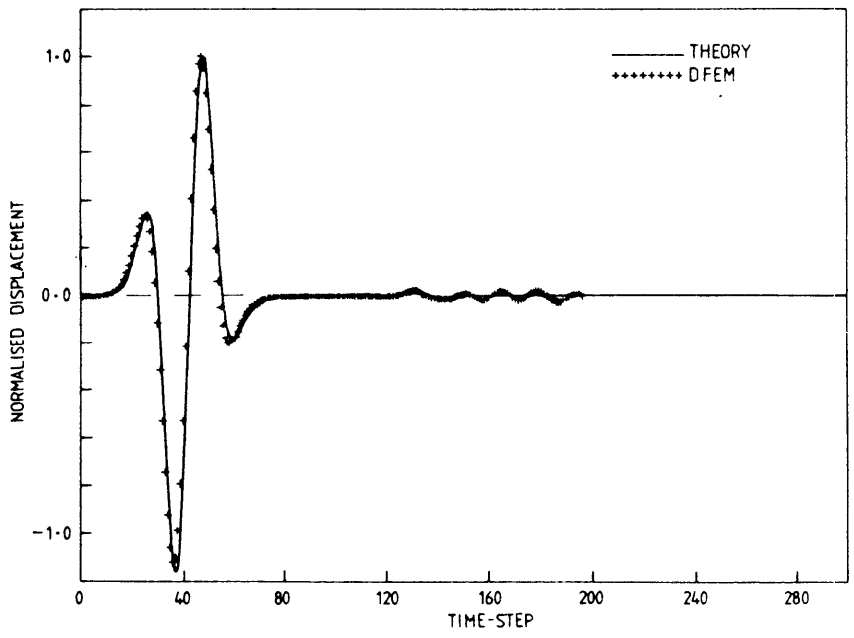

(b)

Figure 26. Displacement response, both theoretical and DFEM at the origin for two source pulses; (a) 4th order Butterworth impulse response and (b) "Gaussian".

5.2.3 Cavity compliances from the DFEM model

As can be seen from the theoretical waveforms for the near field (r = a) and the waveforms for the far-field (r >> a), the waveforms are characterised by a well defined signature (Figures 23 and 26). This signature can be described as consisting of a primary displacement pulse, similar in shape to the source waveform, followed by a train of secondary pulses with amplitude decreasing logarithmically. They are separated by a "dead-band" arising from the approximate time taken for a Rayleigh wave to circuit the cavity. Thus, following transient excitation, the cavity continues to pulse into the surrounding medium as trapped energy circulates around the cavity walls. The energy, retained on the cavity walls as predominantly Rayleigh type modes, is rapidly diminished by radiation damping. Similar conclusions concerning circulating Rayleigh waves have been drawn by Miklowitz (1980)

In the dynamic finite element waveforms, at least the first secondary pulse can be distinguished, although for solution times longer than 200 time-steps, spurious oscillations occur in the solution presumably due to inter-element reflections. Due to its relatively high amplitude, the first secondary pulse is mainly responsible for the mild oscillations in the compliance transfer functions.

As θ increases, the primary pulse decreases in amplitude with respect to the secondary pulse and the pulses tend to merge. However, the total length (in time) of the waveform packet remains approximately constant. This facilitates calculations of compliance transfer functions from the DFEM waveforms using spectral ratio techniques (again using the Fast Fourier transforms of Singleton, 1967). An example of compliance predicted by the DFEM together with the analytical predictions (at $\theta = 0$) is presented in Figure 27.

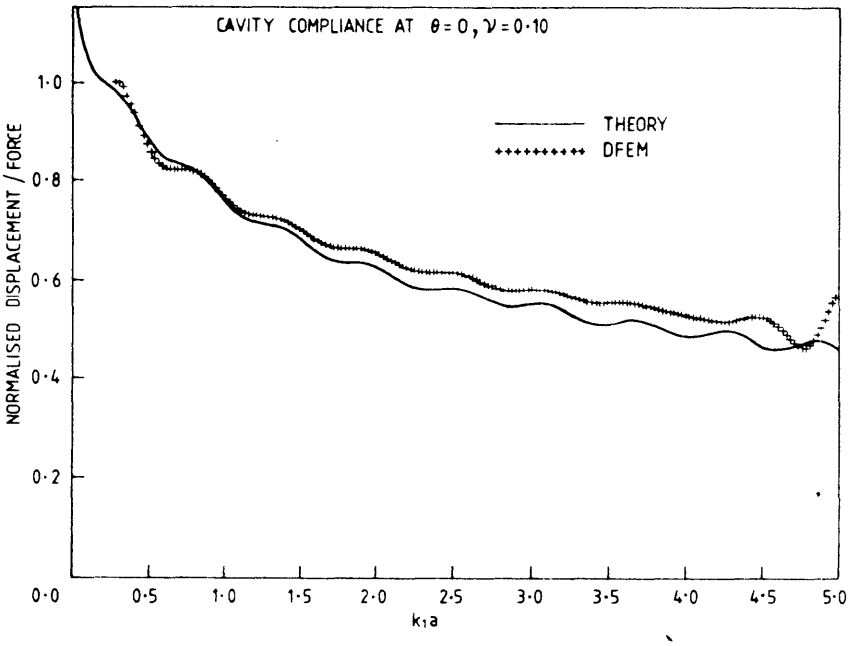

(a)

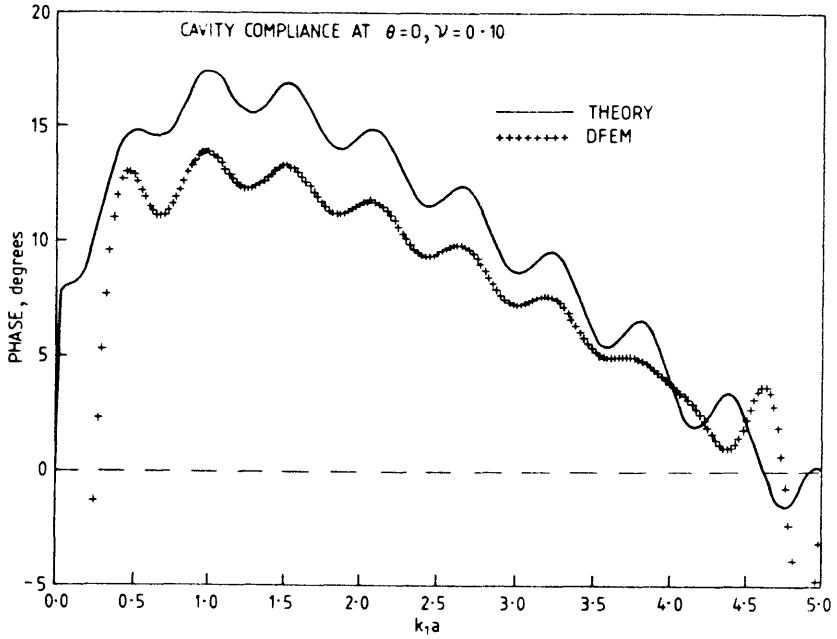

(b)

Figure 27. Cavity compliance transfer functions at $\theta = 0$ predicted from theory and from DFEM spectral ratio results.

6. Steady-state and resonance behaviour of cylindrical cavities in elastic media

The resonance behaviour of cavities in elastic media has been discussed by many authors, particularly by Pao and Mow (1973). However, attention has been largely focused on resonances of fluid-filled cavities with little discussion of resonances in the empty cavity case. For example, Uberall (1977), in his review of resonance scattering, discusses the case of a water filled cavity where as he states "the relatively strong resonances of the water inclusion are superimposed on a *soft* background of cavity wall resonances". (My italics).

The resonances of the empty cavity are governed by the poles of the cavity compliance transfer function as presented in Figure 5 . As shown earlier in this thesis and in Stokes and Siggins (1987), these poles are common to many transfer functions. For each integer value, n, on a particular pole trajectory, the corresponding complex wave-number, x, is the eigenfrequency of the cavity. Eigenfrequencies correspond to natural resonances (normal - modes) and in this case the imaginery component is associated with the radiation damping of that mode, i.e., the damping coefficient for a particular mode is given by the imaginary component of the eigenfrequency.

It can be seen from Figure 5 that eigenfrequencies associated with dominant modes, i.e., those eigenfrequencies with least damping, lie on the Rayleigh branch of the pole trajectories and are followed in importance by contributions from a compressional branch (P1). Table 3 presents some eigenfrequencies from the Rayleigh branch for a cylindrical cavity in an elastic medium with Poisson's ratio equal to 0.1.

Glass (1974) attempted a dynamic finite element solution for low frequencies with rectangular cavities and concluded that his results showed no evidence of cavity resonance. However, the analytical compliance transfer functions presented in Figures 7, together with the corresponding DFEM results, all show evidence of lossy resonance

behaviour with Poisson's ratios equal to 0.1 and 0.25. These effects appear to diminish with increasing Poisson's ratio. The wavenumbers at which these resonant amplifications occur can be conveniently obtained from the positions of maxima in the derivative of compliance phase with respect to wavenumber. Wavenumbers computed in this way, for both analytical and DFEM compliances at $\theta = 0$, are shown in Table 4.

As can be seen from a comparison of Tables 3 and 4, there is an approximate correspondence between the real components of the eigenfrequencies and the frequencies at which resonant amplifications occur in the transfer functions. This demonstrates that the resonances arise from predominantly Rayleigh contributions. The unequal separation between resonances is a result of the dispersive behaviour of Rayleigh waves on curved surfaces such as cavity walls where the wavelengths are of the order of the cavity radius. This was originally predicted by Viktorov, 1958.

The steady-state displacement amplitudes of the cavity walls, as a function of θ, at the above wavenumbers can be considered as the mode-shapes of the cavity. These can be readily obtained from equation (32). Radial mode-shapes (amplitudes) up to $n = 6$ are presented in Figures 28(a) to 28(e) together with the corresponding DFEM results. The DFEM mode shape data were obtained from transfer functions computed using spectral ratio techniques for increments of $\pi/48$ in θ for $0<\theta<\pi$.

Table 3. Eigenfrequencies from the Rayleigh branch for Poisson's ratio equal to 0.1

Mode number (n)	Eigenfrequencies (x)
2	0.3073 - 0.2737i
3	0.8681 - 0.3147i
4	1.4303 - 0.3286i
5	1.9965 - 0.3328i
6	2.5662 - 0.3321i
7	3.1930 - 0.3283i
8	3.7144 - 0.3158i

Table 4. Wavenumbers at which resonant amplifications occur in both analytical and DFEM predicted compliance transfer functions at $\theta = 0$, Poisson's ratio = 0.1.

Maximum (no.)	Wavenumber (k_1a) Analytical	DFEM	Percent error of DFEM results.
2	0.288	-	-
3	0.836	0.800	-4.3
4	1.403	1.364	-2.8
5	1.970	1.940	-1.5
6	2.542	2.513	-1.1
7	3.117	3.083	-1.1
8	3.694	3.642	-1.4

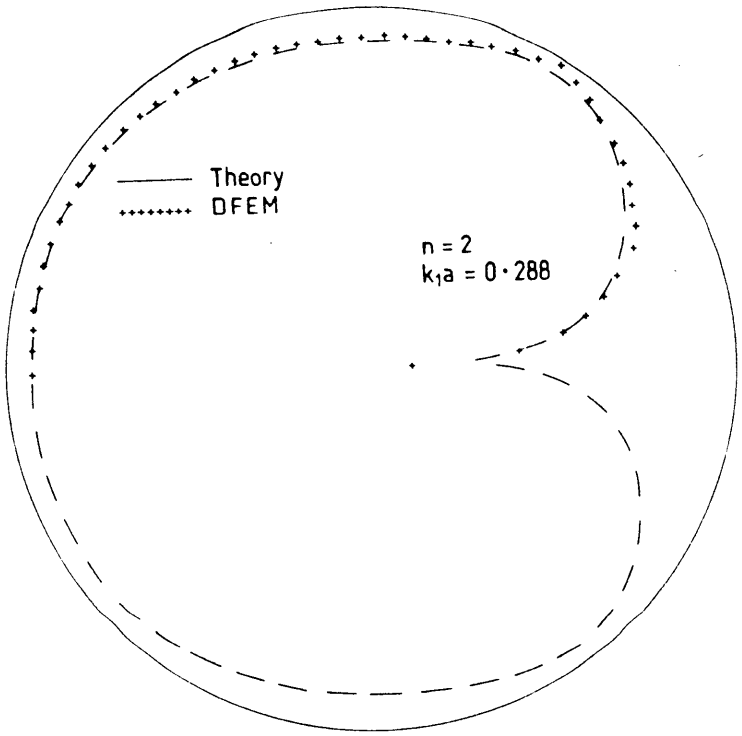

(a)

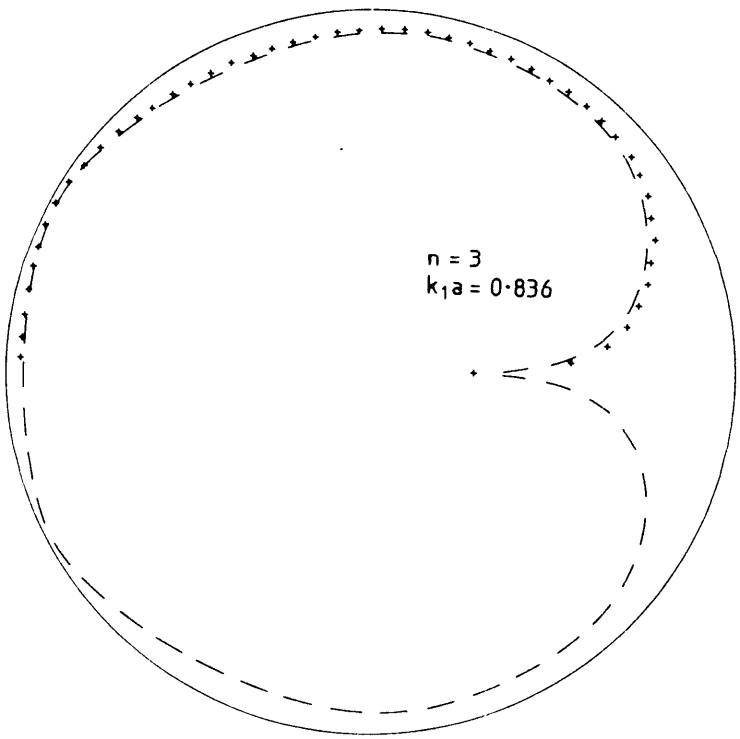

(b)

Figure 28. Radial mode shapes (amplitude) of the cavity wall at "resonance"

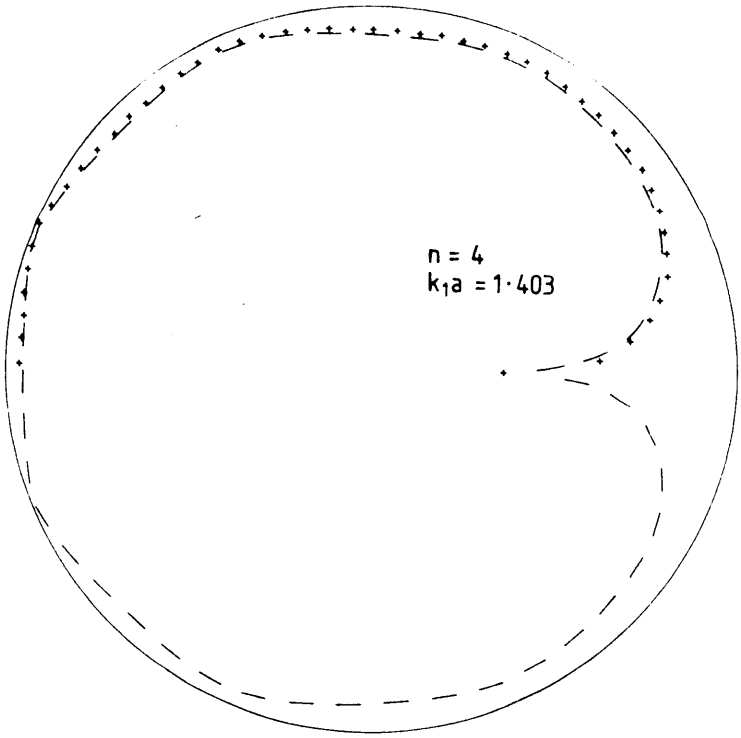

(c)

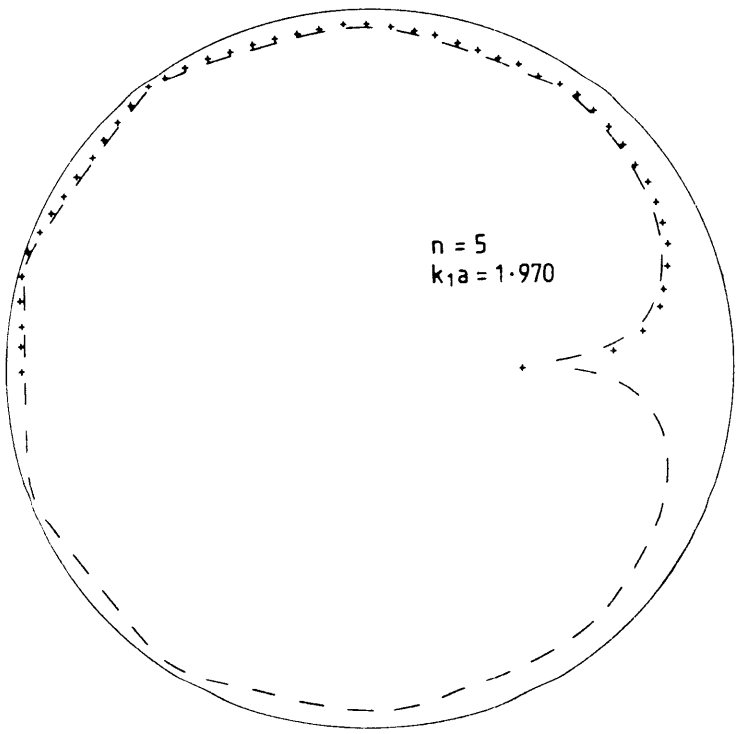

(d)

Figure 28 (continued). Radial mode shapes of the cavity wall at "resonance ".

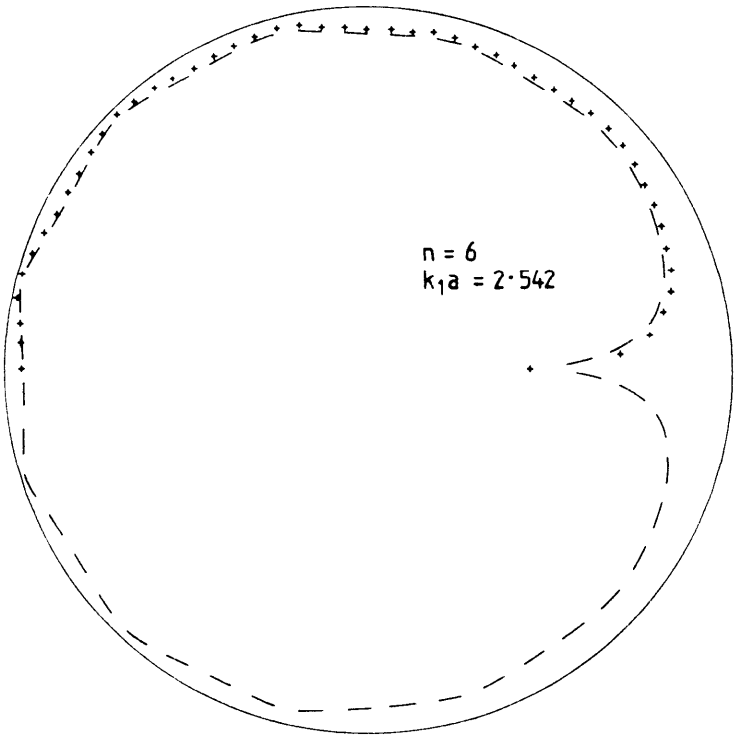

(e)

Figure 28 (continued). Radial mode shapes of the cavity wall at "resonance ".